Marine terraces of the last interglacial period along the Pacific coast of South America (1°N-40°S)

Roland Freisleben[1], Julius Jara-Muñoz[1], Daniel Melnick[2,3], José Miguel Martínez[2,3], Manfred R. Strecker[1]

[1] Institut für Geowissenschaften, Universität Potsdam, 14476 Potsdam, Germany
[2] Instituto de Ciencias de la Tierra, TAQUACH, Universidad Austral de Chile, Valdivia, Chile
[3] Millennium Nucleus The Seismic Cycle Along Subduction Zones, Valdivia, Chile

Correspondence to: Roland Freisleben (freisleb@uni-potsdam.de)

Abstract. Tectonically active coasts are dynamic environments characterized by the presence of multiple marine terraces formed by the combined effects of wave-erosion, tectonic uplift, and sea-level oscillations at glacial-cycle timescales. Well-preserved erosional terraces from the last interglacial sea-level highstand are ideal marker horizons for reconstructing past sea-level positions and calculating vertical displacement rates. We carried out an almost continuous mapping of the last interglacial marine terrace along ~5,000 km of the western coast of South America between 1°N and 40°S. We used quantitatively replicable approaches constrained by published terrace-age estimates to ultimately compare elevations and patterns of uplifted terraces with tectonic and climatic parameters in order to evaluate the controlling mechanisms for the formation and preservation of marine terraces, and crustal deformation. Uncertainties were estimated on the basis of measurement errors and the distance from referencing points. Overall, our results indicate a median elevation of 30.1 m, which would imply a median uplift rate of 0.22 m/ka averaged over the past ~125 ka. The patterns of terrace elevation and uplift rate display high-amplitude (~100–200 m) and long-wavelength (~10^2 km) structures at the Manta Peninsula (Ecuador), the San Juan de Marcona area (central Peru), and the Arauco Peninsula (south-central Chile). Medium-wavelength structures occur at the Mejillones Peninsula and Topocalma in Chile, while short-wavelength (< 10 km) features are for instance located near Los Vilos, Valparaíso, and Carranza, Chile. We interpret the long-wavelength deformation to be controlled by deep-seated processes at the plate interface such as the subduction of major bathymetric anomalies like the Nazca and Carnegie ridges. In contrast, short-wavelength deformation may be primarily controlled by sources in the upper plate such as crustal faulting, which, however, may also be associated with the subduction of topographically less pronounced bathymetric anomalies. Latitudinal differences in climate additionally control the formation and preservation of marine terraces. Based on our synopsis we propose that increasing wave height and tidal range result in enhanced erosion and morphologically well-defined marine terraces in south-central Chile. Our study emphasizes the importance of using systematic measurements and uniform, quantitative methodologies to characterize and correctly interpret marine terraces at regional scales, especially if they are used to unravel tectonic and climatic forcing mechanisms of their formation. This database is an integral part of the World Atlas of Last Interglacial Shorelines (WALIS), published online at http://doi.org/10.5281/zenodo.4309748 (Freisleben et al., 2020).

1. Introduction

Tectonically active coasts are highly dynamic geomorphic environments and they host densely-populated centers and associated infrastructure (Melet et al., 2020). Coastal areas have been episodically affected by the effects of sea-level changes at glacial timescales, modifying the landscape and leaving behind fossil geomorphic markers, such as former paleo-shorelines, and marine terraces (Lajoie, 1986). One of the most prominent coastal landforms are marine terraces that were generated during the protracted last interglacial sea-level highstand that occurred ~125 ka ago (Siddall et al., 2006; Hearty et al., 2007; Pedoja et al., 2011). These terraces are characterized by a higher preservation potential, which facilitates their recognition, mapping, and lateral correlation. Furthermore, because of their high degree of preservation and relatively young age, they have been used to estimate vertical deformation rates at local and regional scales. The relative abundance and geomorphic characteristics of the last interglacial marine terraces make them ideal geomorphic markers with which to reconstruct past sea-level positions and to enable comparisons between distant sites under different climatic and tectonic settings.

The Western South American Coast (WSAC) is a tectonically active region that has been repeatedly affected by megathrust earthquakes and associated surface deformation (Beck et al., 1998; Melnick et al., 2006; Bilek, 2010; Baker et al., 2013). Interestingly, previous studies have shown that despite the broad spectrum of latitudinal climatic conditions and erosional regimes along the WSAC, marine terraces are scattered, but omnipresent along the coast (Ota et al., 1995; Regard et al., 2010; Rehak et al., 2010; Bernhardt et al., 2016; Melnick, 2016; Bernhardt et al., 2017). However, only a few studies on interglacial marine terraces have been conducted along the WSAC, primarily in specific areas where they are best expressed; this has resulted in disparate and inconclusive marine terrace measurements based on different methodological approaches and ambiguous interpretations concerning their origin in a tectonic and climatic context (Hsu et al., 1989; Ortlieb and Macharé, 1990; Hsu, 1992; Macharé and Ortlieb, 1992; Pedoja et al., 2006b; Saillard et al., 2009; Pedoja et al., 2011; Saillard et al., 2011; Rodríguez et al., 2013). This lack of reliable data points has revealed a need to re-examine the last interglacial marine terraces along the WSAC based on standardized methodologies in order to obtain a systematic and continuous record of marine terrace elevations along the coast. This information is crucial in order to increase our knowledge of the climatic and tectonic forcing mechanisms that contributed to the formation and degradation of marine terraces in this region.

Marine terrace sequences at tectonically active coasts are landforms formed by wave erosion and/or accumulation of sediments resulting from the interaction between tectonic uplift and superposed oscillating sea-level changes (Lajoie, 1986; Anderson et al., 1999; Jara-Muñoz et al., 2015). Typically, marine terrace elevations are estimated based on the shoreline angle. The marine terrace morphology comprises a gently inclined erosional or depositional paleo-platform that terminates landward at a steeply sloping paleo-cliff surface. The intersection point between both surfaces represents the approximate sea-level position during the formation of the marine terrace also known as shoreline angle; if coastal uplift is rapid, such uplifting abrasion or depositional surfaces may be preserved in the landscape and remain unaltered by the effects of subsequent sea-level oscillations (Lajoie, 1986).

The analysis of elevation patterns based on shoreline-angle measurements at subduction margins has been largely used to estimate vertical deformation rates and the mechanisms controlling deformation, including the interaction of the upper plate with bathymetric anomalies, the activity of crustal faults in the upper plate, and deep-seated processes such as basal accretion of subducted trench sediments (Taylor et al., 1987; Hsu, 1992; Macharé and Ortlieb, 1992; Ota et al., 1995; Pedoja et al., 2011; Saillard et al., 2011; Jara-Muñoz et al., 2015; Melnick, 2016). The shoreline angle represents a 1D descriptor of the marine terrace elevation, whose measurements are reproducible when using quantitative morphometric approaches (Jara-Muñoz et al., 2016). Furthermore, the estimation of the marine terrace elevations based on shoreline angles can be further improved by quantifying their relationship with paleo-sea level, also known as the indicative meaning (Lorscheid and Rovere, 2019).

In this continental-scale compilation of marine terrace elevations along the WSAC, we present systematically mapped shoreline angles of marine terraces of the last (Eem/Sangamon) interglacial obtained along 5,000 km of coastline between 1°N and 40°S. In this synthesis we rely on chronological constraints from previous regional studies and compilations (Pedoja et al., 2011). For the first time we are able to introduce an almost continuous pattern of terrace elevation and coastal uplift rates at a spatial scale of 10^3 km along the WSAC. Furthermore, in our database we compare tectonic and climatic parameters to elucidate the mechanisms controlling the formation and preservation of marine terraces, and patterns of crustal deformation along the coast. This study was thus primarily intended to provide a comprehensive, standardized database and description of last interglacial marine terrace elevations along the tectonically active coast of South America. This database therefore affords future research into coastal environments to decipher potential tectonic forcings with regard to the deformation and seismotectonic segmentation of the forearc; as such this database will ultimately help to decipher the relationship between upper-plate deformation, vertical motion and bathymetric anomalies and aid in the identification of regional fault motions along pre-existing anisotropies in the South American continental plate. Finally, our database includes information on climate-driving forcing mechanisms that may influence the formation, modification and/or destruction of marine terraces in different climatic sectors along the South American convergent margin. This new database is part of the World Atlas of Last Interglacial Shorelines (WALIS), published online at http://doi.org/10.5281/zenodo.4309748 (Freisleben et al., 2020).

2. Geologic and geomorphic setting of the WSAC

2.1. Tectonic and seismotectonic setting

2.1.1. Subduction geometry and bathymetric features

The tectonic setting of the convergent margin of South America is controlled by subduction of the oceanic Nazca plate beneath the South American continental plate. The convergence rate varies between 66 mm/a in the north (8°S latitude) and 74 mm/a in the south (27°S latitude) (Fig. 1). The convergence azimuth changes slightly from N81.7° toward N77.5° from north to south (DeMets et al., 2010). The South American subduction zone is divided into four major segments with variable subduction angles inferred from the spatial distribution of Benioff seismicity (Barazangi and Isacks, 1976; Jordan et al., 1983) (Fig. 1). The segments beneath northern and central Peru (2°–15°S) and beneath

central Chile (27°–33°S) are characterized by a gentle dip of the subducting plate between 5° and 10° at depths of ~100 km (Hayes et al., 2018), whereas the segments beneath southern Peru and northern Chile (15°–27°S), and beneath southern Chile (33°–45°S) have steeper dips of 25° to 30°. Spatial distributions of earthquakes furthermore indicate a steep-slab subduction segment in Ecuador and southern Colombia (2°S to 5°N), and a flat-slab segment in NW Colombia (north of 5°N) (Pilger, 1981; Cahill and Isacks, 1992; Gutscher et al., 2000; Ramos and Folguera, 2009). Processes that have been inferred to be responsible for the shallowing of the subduction slab include the subduction of large buoyant ridges or plateaus (Espurt et al., 2008) as well as the combination of trenchward motion of thick, buoyant continental lithosphere accompanied by trench retreat (Sobolev and Babeyko, 2005; Manea et al., 2012). Volcanic activity as well as the forearc architecture and distribution of upper-plate deformation further emphasize the location of flat-slab subduction segments (Jordan et al., 1983; Kay et al., 1987; Ramos and Folguera, 2009).

Several high bathymetric features have been recognized on the subducting Nazca plate. The two most prominent bathymetric features being subducted beneath South America are the Carnegie and Nazca aseismic ridges at 0° and 15°S, respectively; they consist of seamounts related to hot-spot volcanism (Gutscher et al., 1999; Hampel, 2002). The 300-km-wide and ~2-km-high Carnegie Ridge subducts roughly parallel with the convergence direction and its geometry should have remained relatively stable beneath the continental plate (Angermann et al., 1999; Gutscher et al., 1999; DeMets et al., 2010; Martinod et al., 2016a). In contrast, the obliquity of the 200-km-wide and 1.5-km-high Nazca Ridge with respect to the convergence direction resulted in 500 km SE-directed migration of its locus of ridge subduction during the last 10 Ma (Hampel, 2002; Saillard et al., 2011; Martinod et al., 2016a). Similarly, smaller aseismic ridges such as the Juan Fernández Ridge and the Iquique Ridge subduct beneath the South American continent at 32°S and 21°S, respectively. The intercepts between these bathymetric anomalies and the upper plate are thought to influence the characteristics of interplate coupling and seismic rupture (Bilek et al., 2003; Wang and Bilek, 2011; Geersen et al., 2015; Collot et al., 2017) and mark the boundaries between flat and steep subduction segments and changes between subduction erosion and accretion (Jordan et al., 1983; von Huene et al., 1997; Ramos and Folguera, 2009) (Fig. 1).

In addition to bathymetric anomalies, several studies have shown that variations in the volume of sediments in the trench may control the subduction regime from an erosional mode to an accretionary mode (von Huene and Scholl, 1991; Bangs and Cande, 1997). In addition, the volume of sediment in the trench has also been hypothesized to influence the style of interplate seismicity (Lamb and Davis, 2003). At the southern Chile margin, thick trench-sediment sequences and a steeper subduction angle correlate primarily with subduction accretion, although the area of the intercept of the continental plate with the Chile Rise spreading center locally exhibits the opposite case (von Huene and Scholl, 1991; Bangs and Cande, 1997). Subduction erosion characterizes the region north of the southern volcanic zone from central and northern Chile to southern Peru (33°–15°S) due to decreasing sediment supply to the trench, especially within the flat-slab subduction segments (Stern, 1991; von Huene and Scholl, 1991; Bangs and Cande, 1997; Clift and Vannucchi, 2004). Clift and Hartley (2007) and Lohrmann et al. (2003) argued for an alternate style of slow tectonic erosion leading to underplating of subducted material below the base of the crustal forearc, synchronous with tectonic erosion beneath the trenchward part of the forearc. For the northern Andes, several authors

also classify the subduction zone as an erosional type (Clift and Vannucchi, 2004; Scholl and Huene, 2007; Marcaillou et al., 2016).

2.1.2. Major continental fault systems in the coastal realm

The South American convergent margin comprises several fault systems with different kinematics, whose presence is closely linked to oblique subduction and the motion and deformation of forearc slivers. Here we summarize the main structures that affect the Pacific coastal areas. North of the Talara bend (5°S), active thrusting and dextral strike-slip faulting dominates the coastal lowlands of Ecuador (e.g., Mache, Bahía, Jipijapa faults), although normal faulting also occurs at Punta Galera (Cumilínche fault) and the Manta Peninsula (Río Salado fault) (Fig. 1). Farther south, normal faulting is active in the Gulf of Guayaquil (Posorja fault) and dextral strike-slip faulting occurs at the Santa Elena Peninsula (La Cruz fault) (Veloza et al., 2012; Costa et al., 2020). The most prominent dextral fault in this region is the 2000-km-long, northeast-striking Dolores-Guayaquil megashear (DGM), which starts in the Gulf of Guayaquil and terminates in the Colombian hinterland east of the range-bounding thrust faults of the Colombian Andes (Veloza et al., 2012; Villegas-Lanza et al., 2016; Costa et al., 2020) (Fig. 1). Normal faults have been described along the coast of Peru at the Illescas Peninsula in the north (6°S), within the El Huevo–Lomas fault system in the San Juan de Marcona area (14.5°–16°S), and within the Incapuquio fault system farther south (17°–18°S) (Veloza et al., 2012; Villegas-Lanza et al., 2016; Costa et al., 2020). The main fault zones of the Chilean convergent margin comprise the Atacama Fault System (AFS) in the Coastal Cordillera extending from Iquique to La Serena (29.75°S, Fig. 1), with predominantly N-S-striking normal faults, which result in relative uplift of their western side (e.g., Mejillones fault, Salar del Carmen fault) (Naranjo, 1987; González and Carrizo, 2003; Cembrano et al., 2007). Coastal fault systems farther south are located in the Altos de Talinay area (30.5°S, Puerto Aldea fault), near Valparaíso (33°S, Quintay and Valparaíso faults), near the Arauco Peninsula (36°–39°S, Santa María and Lanalhue faults), and in between these areas (Topocalma, Pichilemu, Carranza, and Pelluhue faults) (Ota et al., 1995; Melnick et al., 2009; Santibáñez et al., 2019; Melnick et al., 2020; Maldonado et al., 2021) (Fig. 1). However, there is still limited knowledge regarding Quaternary slip rates and kinematics and, most importantly, the location of active faults along the forearc region of South America (Jara-Muñoz et al., 2018; Melnick et al., 2019).

2.2. Climate and geomorphic setting

2.2.1. Geomorphology

The 8000-km-long Andean orogen is a major, hemisphere-scale feature that can be divided into segments with distinctive geomorphic and tectonic characteristics. The principal segments comprise the NNE-SSW trending Colombian-Ecuadorian segment (12°N–5°S), the NW-SE oriented Peruvian segment (5°–18°S), and the N-S trending Chilean segment (18°–56°S) (Jaillard et al., 2000) (Fig. 1). Two major breaks separate these segments; these are the Huancabamba bend in northern Peru and the Arica bend at the Peru-Chile border. The distance of the trench from the WSAC coastline averages 118 km and ranges between 44 and 217 km. The depth of the trench varies between

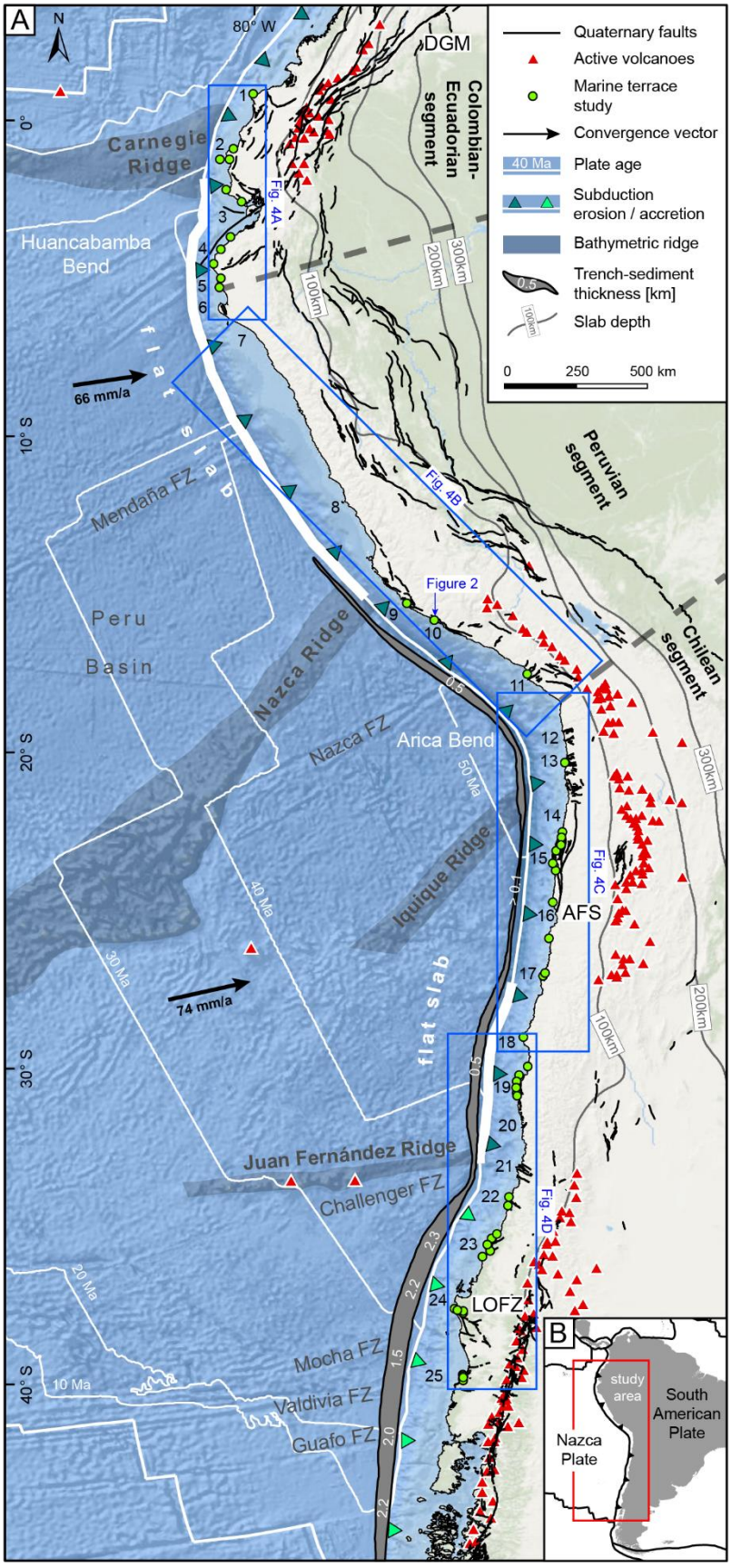

Figure 1. (A) Morphotectonic setting of the South American margin showing major fault systems/crustal faults (Costa et al., 2000; Veloza et al., 2012; Melnick et al., 2020), slab depth (Hayes et al., 2018), and flat-slab subduction segments, active volcanos (Venzke, 2013), bathymetric features of the subducting plate, trench-sediment thickness (Bangs and Cande, 1997), segments of subduction erosion and accretion (Clift and Vannucchi, 2004), plate age (Müller et al., 2008), convergence vectors (DeMets et al., 2010), and marine terrace ages used for lateral correlation. DGM: Dolores-Guayaquil megashear, AFS: Atacama Fault System, LOFZ: Liquiñe-Ofqui Fault Zone, FZ: Fracture Zone, 1: Punta Galera, 2: Manta Pen., 3: Gulf of Guayaquil / Santa Elena Pen., 4: Tablazo Lobitos, 5: Paita Pen., 6: Illescas Pen., 7: Chiclayo, 8: Lima, 9: San Juan de Marcona, 10: Chala Bay, 11: Pampa del Palo, 12: Pisagua, 13: Iquique, 14: Tocopilla, 15: Mejillones Pen., 16: Taltal, 17: Caldera, 18: Punta Choros, 19: Altos de Talinay, 20: Los Vilos, 21: Valparaíso, 22: Topocalma, 23: Carranza, 24: Arauco Pen., 25: Valdivia (World Ocean Basemap: Esri, Garmin, GEBCO, NOAA NGDC, and other contributors). (B) Location of the study area.

2920 and 8177 m (GEBCO Bathymetric Compilation Group, 2020), and the continental shelf has an average width of 28 km (Paris et al., 2016).

In the 50- to 180-km-wide coastal area of the Ecuadorian Andes, where the Western Cordillera is flanked by a structural depression, relief is relatively low (< 300 m asl). The Gulf of Guayaquil (3°S) and the Dolores-Guayaquil megashear separate the northern from the southern forearc units. The coast-trench distance along the Huancabamba bend is quite small (~55–90 km), except for the Gulf of Guayaquil, and the trench east of the Carnegie Ridge is at a relatively shallow depth of ~3.5 km. Farther south, the Peruvian forearc comprises the up to 160-km-wide Coastal Plains in the north and the narrow, 3000-m-high Western Cordillera. While the Coastal plains in north-central Peru are relatively narrow (< 40 km), they widen in southern Peru, and the elevation of the Western Cordillera increases to more than 5000 m (Suárez et al., 1983; Jaillard et al., 2000). The region between the coast and the trench in central Peru (up to 220 km) narrows toward the San Juan de Marcona area (~75 km) near the intercept with the Nazca Ridge, and the relatively deep trench (~6.5 km) becomes shallower (< 5 km) (GEBCO Bathymetric Compilation Group, 2020). Between 18°S and 28°S, the Chilean forearc comprises the 50-km-wide and up to 2700-m-high Coastal Cordillera, which is separated from the Precordillera by the Central Depression. In the flat-slab subduction segment between 27°S and 33°S there is neither a morphotectonic region characterized by a central depression nor active volcanism in the high Andean cordillera (Fig. 1) (Jordan et al., 1983). The Chilean forearc comprises the Coastal Cordillera, which varies in altitude from up to 2000 m at 33°S to 500 m at 46°S, and the Central Depression that separates the forearc from the Main Cordillera. From the Arica bend, where the coast-trench distance is up to 170 km and the trench ~8 km deep, a slight increase in coast-trench distance can be observed in Chile toward the south (~80–130 km), as can a decrease in trench depth to ~4.5 km.

2.2.2. Marine terraces and coastal uplift rates

Wave erosion generates wave-cut terrace levels, while the accumulation of shallow marine sediments during sea-level highstands forms wave-built terraces. Another type of terrace is known as “rasa” and refers to wide shore platforms formed under slow-uplift conditions (< 0.2 m/ka), and the repeated reoccupation of this surface by high sea levels (Regard et al., 2010; Rodríguez et al., 2013; Melnick, 2016). Other studies indicate a stronger influence of climate and rock resistance to erosion compared to marine wave action (Prémaillon et al., 2018). Typically, the formation of Pleistocene marine terraces in the study area occurred during interglacial and interstadial relative sea-level highstands that were superposed on the uplifting coastal areas; according to the Quaternary oxygen-isotope curve defining warm and cold periods, high Quaternary sea levels have been correlated with warm periods and are denoted with the odd-numbered Marine Isotope Stages (MIS) (Lajoie, 1986; Shackleton et al., 2003).

Along the WSAC, staircase-like sequences of multiple marine terraces are preserved nearly continuously along the coast. These terraces comprise primarily wave-cut surfaces that are frequently covered by beach ridges of siliciclastic sediments and local accumulations of carbonate bioclastic materials (Ota et al., 1995; Saillard et al., 2009; Rodríguez et al., 2013; Martinod et al., 2016b). Rasa surfaces exist in the regions of southern Peru and northern Chile (Regard et al., 2010; Rodríguez et al., 2013; Melnick, 2016). Particularly the well-preserved MIS-5e terrace level has been largely

used as a strain marker in the correlation of uplifted coastal sectors due to its lateral continuity and high potential for preservation. Global observations of sea-level fluctuations during MIS-5 allow to differentiate between three second-order highstands at 80 ka (5a), 105 ka (5c), and 128 to 116 ka (5e) with paleo-sea levels of -20 m for both of the younger and +3 ± 3 m for the oldest highstand (Stirling et al., 1998; Siddall et al., 2006; Hearty et al., 2007; Rohling et al., 2009; Pedoja et al., 2011), although glacio-isostatic adjustments (GIA) can cause local differences of up to 30 m (Simms et al., 2016; Creveling et al., 2017). The database generated in this study is based exclusively in the last interglacial marine terraces exposed along the WSAC, between Ecuador and Southern Chile (1°S to 40°S). In the following section we present a brief review of previously studied marine terrace sites in this area.

Paleo-shoreline elevations of the last interglacial (MIS-5e) in Ecuador are found at elevations of around 45 ± 2 m asl in Punta Galera (Esmeraldas area), 43–57 ± 2 m on the Manta Peninsula and La Plata Island, and 15 ± 5 m asl on the Santa Elena Peninsula (Pedoja et al., 2006b; Pedoja et al., 2006a). In northern Peru, MIS-5e terraces have been described at elevations of 18–31 m asl for the Tablazo Lobitos (Cancas and Mancora areas), at 25 ± 5 m asl on the Paita Peninsula, and at 18 ± 3 m asl on the Illescas Peninsula and the Bay of Bayovar (Pedoja et al., 2006b). Farther south, MIS-5e terraces are exceptionally high in the San Juan de Marcona area immediately south of the subducting Nazca Ridge, with maximum elevations of 80 m at the Cerro Tres Hermanas and 105 m at the Cerro El Huevo (Hsu et al., 1989; Ortlieb and Macharé, 1990; Saillard et al., 2011). The Pampa del Palo region in southern Peru exhibits relatively thick vertical stacks of shallow marine terrace deposits related to MIS-7, 5e (~20 m), and 5c that may indicate a different geodynamic behavior compared to adjacent regions (Ortlieb et al., 1996b). In central and northern Chile, the terrace levels of the last interglacial occur at 250–400 m, 150–240 m, 80–130 m, and 30–40 m, and in southern Chile at 170–200 m, 70 m, 20–38 m, 8–10 m (Fuenzalida et al., 1965). Specifically, between 24°S and 32°S, paleo-shoreline elevations of the last interglacial (MIS-5e) range between 25 and 45 m (Ota et al., 1995; Saillard et al., 2009; Martinod et al., 2016b). Shore platforms are higher in the Altos de Talinay area (30.3°–31.3°S), but are small, poorly preserved, and terminate at a high coastal scarp between 26.75°S and 24°S (Martinod et al., 2016b). Shoreline-angle elevations between 34° and 38°S (along the Maule seismotectonic segment) vary from high altitudes in the Arauco and Topocalma areas (200 m) to moderate elevations near Caranza (110 m), and very low elevations in between (15 m) (Melnick et al., 2009; Jara-Muñoz et al., 2015).

Coastal uplift-rate estimates along the WSAC mainly comprise calculations for the Talara Arc, the San Juan de Marcona area, the Mejillones Peninsula, the Altos de Talinay area, and several regions in south-central Chile. Along the Talara Arc (6.5°S to 1°N), marine terraces of the Manta Peninsula and La Plata Island in central Ecuador indicate the most pronounced uplift rates of 0.31 to 0.42 m/ka since MIS-5e, while similar uplift rates are documented to the north in the Esmeraldas area (0.34 m/ka), and lower ones to the south at the Santa Elena Peninsula (0.1 m/ka). In northern Peru, last interglacial uplift rates are relative low, ranging from 0.17–0.21 m/ka for the Tablazo Lobitos and 0.16 m/ka for the Paita Peninsula, to 0.12 m/ka for the Bay of Bayovar and the Illescas Peninsula (Pedoja et al., 2006b; Pedoja et al., 2006a). Marine terraces on the continental plate above the subducting Nazca Ridge (13.5°–15.6°S) record variations in uplift rate where the coastal forearc above the northern flank of the ridge is either stable or has undergone net subsidence (Macharé and Ortlieb, 1992). The coast above the ridge crest is rising at about 0.3 m/ka and the coast

above the southern flank (San Juan de Marcona) is uplifting at a rate of 0.5 m/ka (Hsu, 1992) or even 0.7 m/ka (Ortlieb and Macharé, 1990) for at least the last 125 ka. Saillard et al. (2011) state that long-term regional uplift in the San Juan de Marcona area has increased since about 800 ka related to the southward migration of the Nazca Ridge, and ranges from 0.44 to 0.87 m/ka. The Pampa del Palo area in southern Peru rose more slowly or was even down-faulted and had subsided with respect to the adjacent coastal regions (Ortlieb et al., 1996b). These movements ceased after the highstand during the MIS-5e and slow uplift rates of approximately 0.16 m/ka have characterized the region since 100 ka (Ortlieb et al., 1996b). In northern Chile (24°–32°S), uplift rates for the Late Pleistocene average around 0.28 ± 0.15 m/ka (Martinod et al., 2016b), except for the Altos de Talinay area, where pulses of rapid uplift occurred during the Middle Pleistocene (Ota et al., 1995; Saillard et al., 2009; Martinod et al., 2016b). The Central Andean rasa (15°–33°S) and Lower to Middle Pleistocene shore platforms – which are also generally wider – indicate a period of tectonic stability or subsidence followed by accelerated and spatially continuous uplift after ~400 ka (MIS-11) (Regard et al., 2010; Rodríguez et al., 2013; Martinod et al., 2016b). However, according to Melnick (2016), the Central Andean rasa has experienced slow and steady long-term uplift with a rate of 0.13 ± 0.04 m/ka during the Quaternary, predominantly accumulating strain through deep earthquakes at the crust-mantle boundary (Moho) below the locked portion of the plate interface. The lowest uplift rates occur at the Arica bend and increase gradually southward; the highest values are attained along geomorphically distinct peninsulas (Melnick, 2016). In the Maule segment (34°-38°S), the mean uplift rate for the MIS-5 terrace level is 0.5 m/ka, exceeded only in the areas of Topocalma, Carranza, and Arauco, where it amounts to 1.6 m/ka (Melnick et al., 2009; Jara-Muñoz et al., 2015). Although there are several studies of marine terraces along the WSAC, these are isolated and based on different methodological approaches, mapping and leveling resolution, as well as dating techniques, which makes regional comparisons and correlations difficult in the context of the data presented here.

2.2.3. Climate

Apart from latitudinal temperature changes, the present-day morphotectonic provinces along the South American margin have a pronounced impact on the precipitation gradients on the west coast of South America. Since mountain ranges are oriented approximately perpendicular to moisture-bearing winds, they affect both flanks of the orogen (Strecker et al., 2007). The regional-scale pattern of wind circulation is dominated by westerly winds at subtropical/extratropical latitudes primarily up to about 27°S (Garreaud, 2009). However, anticyclones over the South Pacific result in winds blowing from the south along the coast between 35°S and 10°S (Garreaud, 2009). The moisture in the equatorial Andes (Ecuador and Colombia) and in the areas farther south (27°S) is fed by winds from the Amazon basin and the Gulf of Panama, resulting in rainfall mainly on the eastern flanks of the mountain range (Bendix et al., 2006; Bookhagen and Strecker, 2008; Garreaud, 2009). The Andes of southern Ecuador, Peru, and northern Chile are dominated by a rain-shadow effect that causes aridity within the Andean Plateau (Altiplano-Puna), the Western Cordillera, and the coastal region (Houston and Hartley, 2003; Strecker et al., 2007; Garreaud, 2009). Furthermore, the aridity is exacerbated by the effects of the cold Humboldt current, which prevents humidity from the Pacific from penetrating inland (Houston and Hartley, 2003; Garreaud, 2009; Coudurier-Curveur et al., 2015). The precipitation gradient reverses between 27°S and 35°S, where the Southern Hemisphere Westerlies cause abundant rainfall on the

western flanks of the Coastal and Main cordilleras (Garreaud, 2009). Martinod et al. (2016b) proposed that latitudinal differences in climate largely influence coastal morphology, specifically the formation of high coastal scarps that prevent the development of extensive marine terrace sequences. However, the details of this relationship have not been conclusively studied along the full extent of the Pacific coast of South America.

3. Methods

We combined – and describe in detail below – bibliographic information, different topographic data sets, and uniform morphometric and statistical approaches to assess the elevation of marine terraces and accompanying vertical deformation rates along the western South American margin.

3.1. Mapping of marine terraces

Marine terraces are primarily described based on their elevation, which is essential for determining vertical deformation rates. The measurements of the marine terrace elevations of the last interglacial were performed using TanDEM-X topography (12 and 30 m horizontal resolution) (German Aerospace Center (DLR), 2018), and digital terrain models from LiDAR (1, 2.5, and 5 m horizontal resolution). The DEMs were converted to orthometric heights by subtracting the EGM2008 geoid and projected in UTM using the World Geodetic System (WGS1984) using zone 19S for Chile, zone 18S for southern/central Peru, and zone 17S for northern Peru/Ecuador.

To trace the MIS-5 shoreline, we mapped its inner edge along the west coast of South America based on slope changes on TanDEM-X topography at the foot of paleo-cliffs (Jara-Muñoz et al., 2016) (Fig. 2A and B). To facilitate mapping, we used slope and hillshade maps. We correlated the results of the inner-edge mapping with the marine terraces catalog of Pedoja et al. (2011) and references therein (section 2.2.2, Table 1). Further references used to validate MIS-5e terrace heights include Victor et al. (2011) for the Pampa de Mejillones, Martinod et al. (2016b) for northern Chile, and Jara-Muñoz et al. (2015) for the area between 34° and 38°S. We define the term “referencing point” for these previously published terrace heights and age constraints. The referencing point with the shortest distance to the location of our measurements served as a topographical and chronological benchmark for mapping the MIS-5 terrace in the respective areas. In addition, this distance is used to assign a quality rating to our measurements.

In addition to MIS-5e, we also mapped MIS-5c in areas with high uplift rates such as at the Manta Peninsula, San Juan de Marcona, Topocalma, Carranza, and Arauco. Although we observed a terrace level correlated to MIS-5a in the Marcona area, we excluded this level from the database due to its limited preservation at other locations and lack of chronological constraints. Our assignment of mapped terrace levels to MIS-5c is primarily based on age constraints by Saillard et al. (2011) for the Marcona area and Jara-Muñoz et al. (2015) for the area between 34° and 38°S. However, in order to evaluate the possibility that our correlation with MIS-5c is flawed, we estimated uplift rates for the lower terraces by assigning them tentatively to either MIS-5a or MIS-5c. We interpolated the uplift rates derived from the MIS-5e level at the sites of the lower terraces and compared the differences (Figure 3A). If we infer that uplift rates were constant in time at each site throughout the three MIS-5 substages, the comparison suggests these

lower terrace levels correspond to MIS-5c because of the smaller difference in uplift rate, rather than to MIS-5a (Figure 3B).

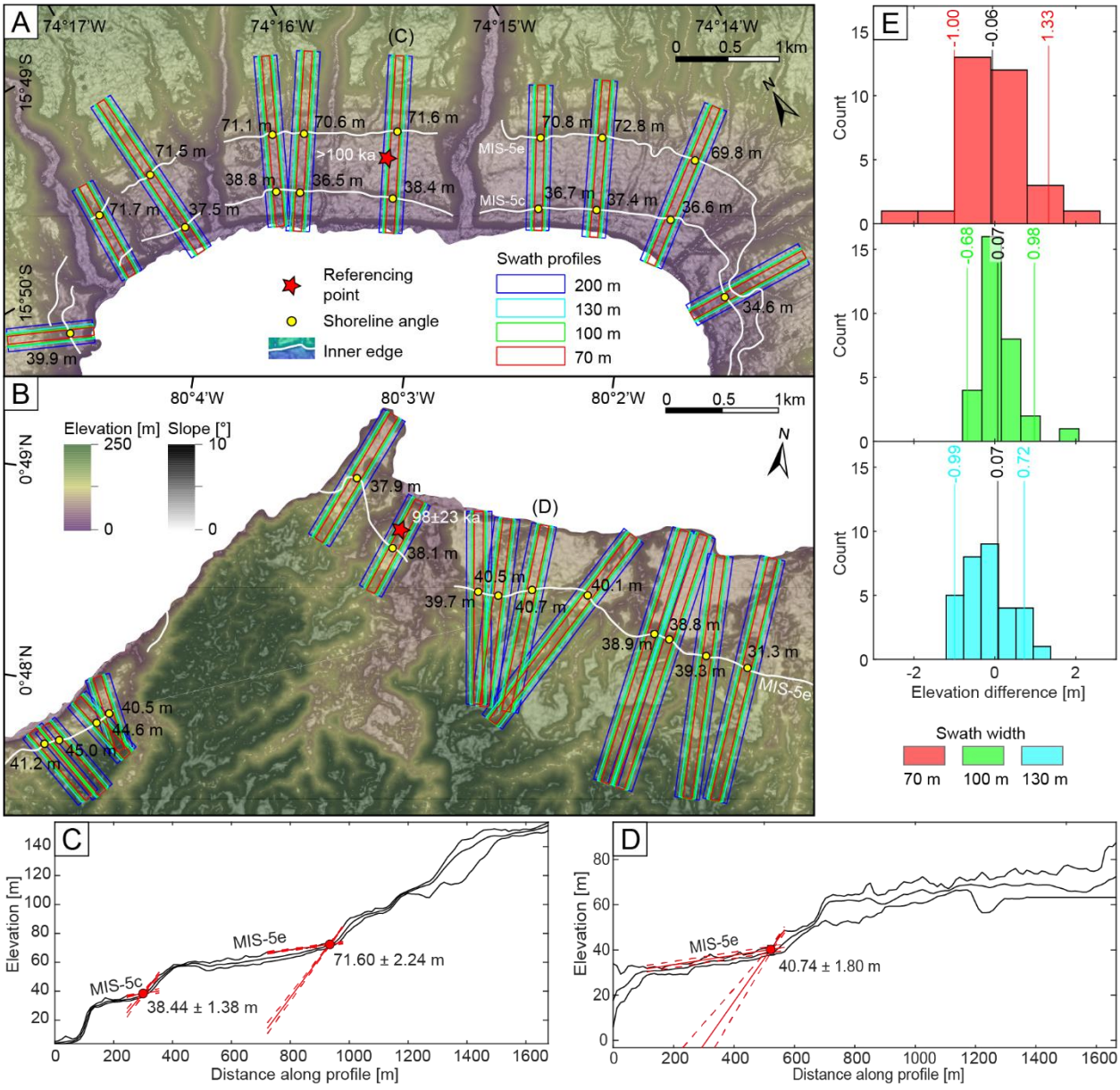

Figure 2. Orthometrically corrected TanDEM-X and slope map of (A) Chala Bay in south-central Peru and (B) Punta Galera in northern Ecuador with mapped inner shoreline edges of the MIS-5e and 5c terrace levels. Colored rectangles represent swath-profile boxes of various widths that were placed perpendicular to the inner edges for the subsequent estimation of terrace elevation in TerraceM. The red star indicates the referencing point with the age constraint for the respective area (Pedoja et al., 2006b; Saillard, 2008). (C) and (D) Estimation of the shoreline-angle elevation in TerraceM by intersecting linear-regression fits of the paleo-cliff and paleo-platform (200-m-wide swath profiles). (E) Histograms of elevation differences measured in both areas for various swath widths (70 m, 100 m, and 130 m) with respect to the 200-m-wide reference swath profile (blue). Vertical lines indicate median values and standard deviations (2σ).

Table 1. Age constraints used for mapping of the inner edge of MIS-5 and for verifying our terrace-elevation measurements. This compilation is mainly based on the terrace catalog of Pedoja et al. (2011); added references include Victor et al. (2011) for Pampa de Mejillones, Martinod et al. (2016b) for northern Chile, and Jara-Muñoz et al. (2015) for south-central Chile. Absolute ages refer to MIS-5e marine terraces, unless otherwise specified; inferred ages refer to their associated MIS. IRSL: Infrared Stimulated Luminescence, AAR: Amino-Acid Racemization, CRN: Cosmogenic Radionuclides, ESR: Electron Spin Resonance.

Country	Location	Lat.	Long.	Dating method	Confidence	Reference	Age [ka]
Ecuador	Galera	0.81	-80.03	IRSL	5	Pedoja et al., 2006b	98±23
Ecuador	Manta	-0.93	-80.66	IRSL, U/Th	5	Pedoja et al., 2006b	76±18, 85±1
Ecuador	La Plata	-1.26	-81.07	U/Th	5	Pedoja et al., 2006b	104±2
Ecuador	Manta	-1.27	-80.78	IRSL	5	Pedoja et al., 2006b	115±23
Ecuador	Santa Elena	-2.21	-80.88	U/Th	5	Pedoja et al., 2006b	136±4, 112±2
Ecuador	Puna	-2.60	-80.40	U/Th	5	Pedoja et al., 2006b	98±3, 95±0
Peru	Cancas	-3.72	-80.75	Morphostratigraphy	5	Pedoja et al., 2006b	~125
Peru	Mancora/ Lobitos	-4.10	-81.05	Morphostratigraphy	5	Pedoja et al., 2006b	~125
Peru	Talara	-4.56	-81.28	Morphostratigraphy	5	Pedoja et al., 2006b	~125
Peru	Paita	-5.03	-81.06	Morphostratigraphy	5	Pedoja et al., 2006b	~125
Peru	Bayovar/ Illescas	-5.31	-81.10	IRSL	5	Pedoja et al., 2006b	111±6
Peru	Cerro Huevo	-15.31	-75.17	CRN	5	Saillard et al., 2011	228±28 (7e)
Peru	Chala Bay	-15.85	-74.31	CRN	5	Saillard, 2008	> 100
Peru	Ilo	-17.55	-71.37	AAR	5	Ortlieb et al., 1996b; Hsu et al., 1989	~125, ~105
Chile	Punta Lobos	-20.35	-70.18	U/Th, ESR	5	Radtke, 1989	~125
Chile	Cobija	-22.55	-70.26	Morphostratigraphy	4	Ortlieb et al., 1995	~125, ~105
Chile	Michilla	-22.71	-70.28	AAR	3	Leonard & Wehmiller, 1991	~125
Chile	Hornitos	-22.85	-70.30	U/Th	5	Ortlieb et al., 1996a	108±1, 118±6
Chile	Chacaya	-22.95	-70.30	AAR	5	Ortlieb et al., 1996a	~125
Chile	Pampa Mejillones	-23.14	-70.45	U/Th	5	Victor et al., 2011	124±3
Chile	Mejillones/ Punta Jorge	-23.54	-70.55	U/Th, ESR	3	Radtke, 1989	~125
Chile	Coloso	-23.76	-70.46	ESR	3	Schellmann & Radtke, 1997	106±3
Chile	Punta Piedras	-24.76	-70.55	CRN	5	Martinod et al., 2016b	138±15
Chile	Esmeralda	-25.91	-70.67	CRN	5	Martinod et al., 2016b	79±9
Chile	Caldera	-27.01	-70.81	U/Th, ESR	5	Marquardt et al., 2004	~125
Chile	Bahia Inglesa	-27.10	-70.85	U/Th, ESR	5	Marquardt et al., 2004	~125
Chile	Caleta Chanaral	-29.03	-71.49	CRN	5	Martinod et al., 2016b	138±0
Chile	Coquimbo	-29.96	-71.34	AAR	5	Leonard & Wehmiller, 1992; Hsu et al., 1989	~125
Chile	Punta Lengua de Vaca	-30.24	-71.63	U/Th	5	Saillard et al., 2012	95±2 (5c)
Chile	Punta Lengua de Vaca	-30.30	-71.61	U/Th	5	Saillard et al., 2012	386±124 (11)
Chile	Quebrada Palo Cortado	-30.44	-71.69	CRN	5	Saillard et al., 2009	149±10

Chile	Rio Limari	-30.63	-71.71	CRN	5	Saillard et al., 2009	318±30 (9c)
Chile	Quebrada de la Mula	-30.79	-71.70	CRN	5	Saillard et al., 2009	225±17 (7e)
Chile	Quebrada del Teniente	-30.89	-71.68	CRN	5	Saillard et al., 2009	678±51 (17)
Chile	Puertecillo	-34.09	-71.94	IRSL	5	Jara-Munoz et al., 2015	87±7 (5c)
Chile	Pichilemu	-34.38	-71.97	IRSL	5	Jara-Munoz et al., 2015	106±9 (5c)
Chile	Putu	-35.16	-72.25	IRSL	5	Jara-Munoz et al., 2015	85±8 (5c)
Chile	Constitucion	-35.40	-72.49	IRSL	5	Jara-Munoz et al., 2015	105±8 (5c)
Chile	Constitucion	-35.44	-72.47	IRSL	5	Jara-Munoz et al., 2015	124±11
Chile	Carranza	-35.58	-72.61	IRSL	5	Jara-Munoz et al., 2015	67±6 (5c)
Chile	Carranza	-35.64	-72.54	IRSL	5	Jara-Munoz et al., 2015	104±9
Chile	Pelluhue	-35.80	-72.54	IRSL	5	Jara-Munoz et al., 2015	112±10
Chile	Pelluhue	-35.80	-72.55	IRSL	5	Jara-Munoz et al., 2015	102±9 (5c)
Chile	Curanipe	-35.97	-72.78	IRSL	5	Jara-Munoz et al., 2015	265±29
Chile	Arauco	-37.62	-73.67	IRSL	5	Jara-Munoz et al., 2015	89±9 (5c)
Chile	Arauco	-37.68	-73.57	CRN	5	Melnick et al., 2009	127±13
Chile	Arauco	-37.71	-73.39	CRN	5	Melnick et al., 2009	133±14
Chile	Arauco	-37.76	-73.38	CRN	5	Melnick et al., 2009	130±13
Chile	Cerro Caleta Curiñanco	-39.72	-73.40	Tephrochronology	4	Pino et al., 2002	~125
Chile	South Curiñanco	-39.76	-73.39	Tephrochronology	4	Pino et al., 2002	~125
Chile	Valdivia	-39.80	-73.39	Tephrochronology	4	Pino et al., 2002	~125
Chile	Camping Bellavista	-39.85	-73.40	Tephrochronology	4	Pino et al., 2002	~125
Chile	Mancera	-39.89	-73.39	Tephrochronology	5	Silva, 2005	~125

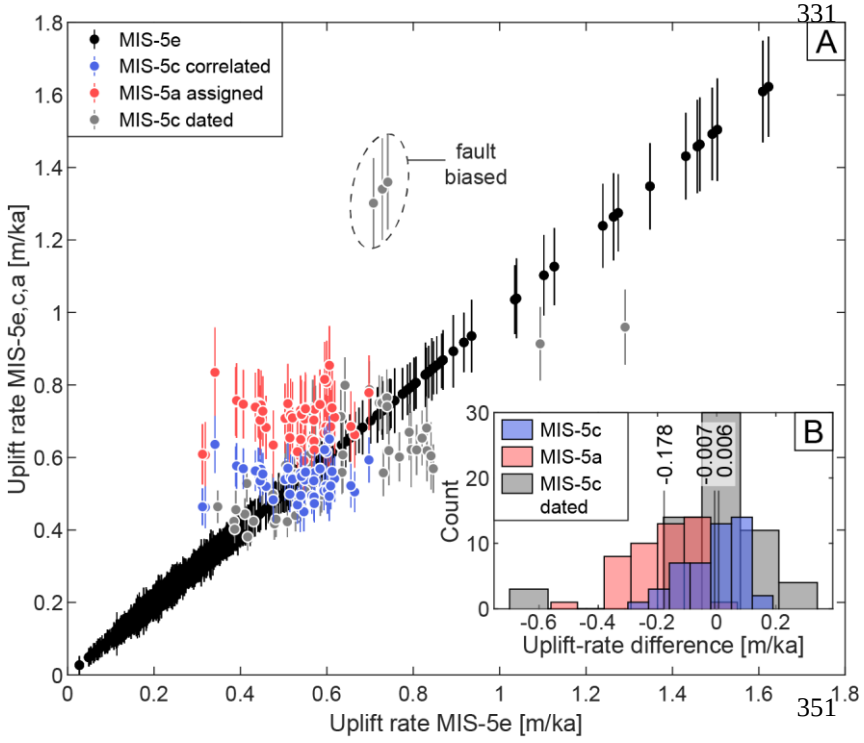

Figure 3. Comparison of MIS-5 uplift-rate estimates. (A) Uplift rates derived by correlating mapped terrace occurrences located immediately below the MIS-5e level to either MIS-5c (blue) or MIS-5a (red) with respect to MIS-5e uplift rates. Marine terraces correlated to MIS-5c by an age constraint are plotted in gray color. (B) Histograms of differences between MIS-5a or MIS-5c uplift rates and MIS-5e uplift rates. Vertical lines show median uplift-rate differences. See section 2.2.2. for relative sea-level elevations of MIS-5a, 5c, 5e.

A rigorous assessment of marine terrace elevations is crucial for determining accurate vertical deformation rates. Since fluvial degradation and hillslope processes subsequent to abandonment of marine terraces may alter terrace morphology (Anderson et al., 1999; Jara-Muñoz et al., 2015), direct measurements of terrace elevations at the inner edge (foot of the paleo-cliff) may result in overestimation of the terrace elevations and vertical deformation rates (Jara-Muñoz et al., 2015). To precisely measure the shoreline-angle elevations of the MIS-5 terrace level, we used a profile-based approach in TerraceM, a graphical user interface in MATLAB® (Jara-Muñoz et al., 2016); www.terracem.com. We placed swath profiles of variable width perpendicular to the previously mapped inner edge, which were used by the TerraceM algorithm to extract maximum elevations to avoid areas of fluvial incision (Fig. 2A and B). For the placement of the swath profiles we tried to capture a local representation of marine terrace topography with a sufficiently long, planar paleo-platform, and a sufficiently high paleo-cliff, simultaneously avoiding topographic disturbance, such as colluvial wedges or areas affected by incision. North of Caleta Chañaral (29°S), we used swath profiles of 200 m width, although we occasionally used 100-m-wide profiles for narrow terrace remnants. South of 29°S, we used swath widths of 130 and 70 m. The width was chosen based on fluvial drainage densities that are associated with precipitation gradients. Sensitivity tests comparing shoreline-angle measurements from different swath widths in the Chala Bay and at Punta Galera show only minimal vertical deviations of less than 0.5 m (Fig. 2E). The sections of these profiles, which represent the undisturbed paleo-platform and paleo-cliff areas, were picked manually and fitted by linear regression. The extrapolated intersection between both regression lines ultimately allowed us to determine the buried shoreline-angle elevation and associated uncertainty, which is derived from the 95% confidence interval (2σ) of both regressions (Fig. 2C and D). In total, we measured 1843 MIS-5e and 110 MIS-5c shoreline-angle elevations. To quantify the paleo-position of the relative sea-level elevation and the involved uncertainty for the WALIS database, we calculated the indicative meaning for each marine terrace measurement using the IMCalc software from Lorscheid and Rovere (2019). The indicative meaning comprises the range between the lower and upper limits of sea-level formation – the indicative range – as well as its mathematically averaged position, which corresponds to the reference water level (Lorscheid and Rovere, 2019). Table 2 documents the medians and standard deviations of these values for four extensive regions along the WSAC.

Table 2. Median values and standard deviations (2σ) representing the indicative meaning along the WSAC. The four sectors were chosen based on their main geomorphic characteristics (see results section).

	Upper limit of modern analog [m]	Lower limit of modern analog [m]	Reference water level [m]	Indicative range [m]
Ecuador and northern Peru	2.89 ± 0.16	-1.78 ± 0.47	0.54 ± 0.21	4.66 ± 0.65
Central and southern Peru	2.98 ± 0.31	-3.05 ± 0.52	-0.03 ± 0.11	6.06 ± 0.90
Northern Chile	3.01 ± 0.15	-2.89 ± 0.30	0.06 ± 0.08	5.90 ± 0.51
Central Chile	3.21 ± 0.19	-3.03 ± 0.38	0.07 ± 0.11	6.25 ± 0.60

To quantify the reliability and consistency of our shoreline-angle measurements, we developed a quality rating from low (1) to high (5) confidence. Equation 1 illustrates how we calculated the individual parameters and the overall quality rating:

Equation 1: Quality rating.

$$QR = 1 + 2.4 * \left(\frac{C_{RP}}{\max(C_{RP})} * \left(1 - \frac{D_{RP}}{\max(D_{RP})}\right)\right)^{e} + 1.2 * \left(1 - \frac{E_T}{\max(E_T)}\right) + 0.4 * 1.2 * \left(1 - \frac{R}{\max(R)}\right)$$

The four parameters included in our quality rating (QR) comprise a) the distance to the nearest referencing point (D_{RP}), b) the confidence of the referencing point based on the dating method used by previous studies (C_{RP}) (Pedoja et al., 2011), c) the measurement error in TerraceM (E_T), and (d) the pixel-scale resolution of the topographic data set (R) (Fig. 4). We did not include the error that results from the usage of different swath widths, since the calculated elevation difference with respect to the most frequently used 200 m swath width is very low (< 0.5 m) (Fig. 2E). From the reference points we only used data points with a confidence value of 3 or greater (1 – poor, 5 – very good) based on the previous qualification of Pedoja et al. (2011). The confidence depends mainly on the reliability of the dating method, but can be increased by good age constraints of adjacent terrace levels or detailed morphostratigraphic correlations, such as in Chala Bay (Fig. 2A) (Goy et al., 1992; Saillard, 2008). We further used this confidence value to quantify the quality of the age constraints in the WALIS template.

To account for the different uncertainties of the individual parameters in the QR, we combined and weighted the parameters D_{RP} and C_{RP} in a first equation claiming 60% of the final QR, E_T in a second and R in a third equation weighted 30% and 10%, respectively. We justify these percentages by the fact that the distance and confidence to the nearest referencing point is of utmost importance for identifying the MIS-5e terrace level. The measurement error represents how well the mapping of the paleo-platform and paleo-cliff resulted in the shoreline-angle measurement, while the topographic resolution of the underlying DEM only influences the precise representation of the actual topography and has little impact on the measurement itself. The coefficient assigned to the topographic resolution is multiplied by a factor of 1.2 in order to maintain the possibility of a maximum QR for a DEM resolution of 5 m. Furthermore, we added an exponent to the first part of the equation to reinforce low confidence and/or high distance of the referencing point for low quality ratings. The exponent adjusts the QR according to the distribution of distances from referencing points, which follows an exponential relationship (Fig. 4D).

The influence of each parameter to the quality rating can be observed in Fig. 4. We observe that for high D_{RP} values the QR becomes constant; likewise, the influence of QR parameters becomes significant for QR values higher than 3. We justify the constancy of the QR for high D_{RP} values (> 300 km) by the fact that most terrace measurements have D_{RP} values below 200 km (Fig. 4D). The quality rating is then used as a descriptor of the confidence of marine terrace-elevation measurements.

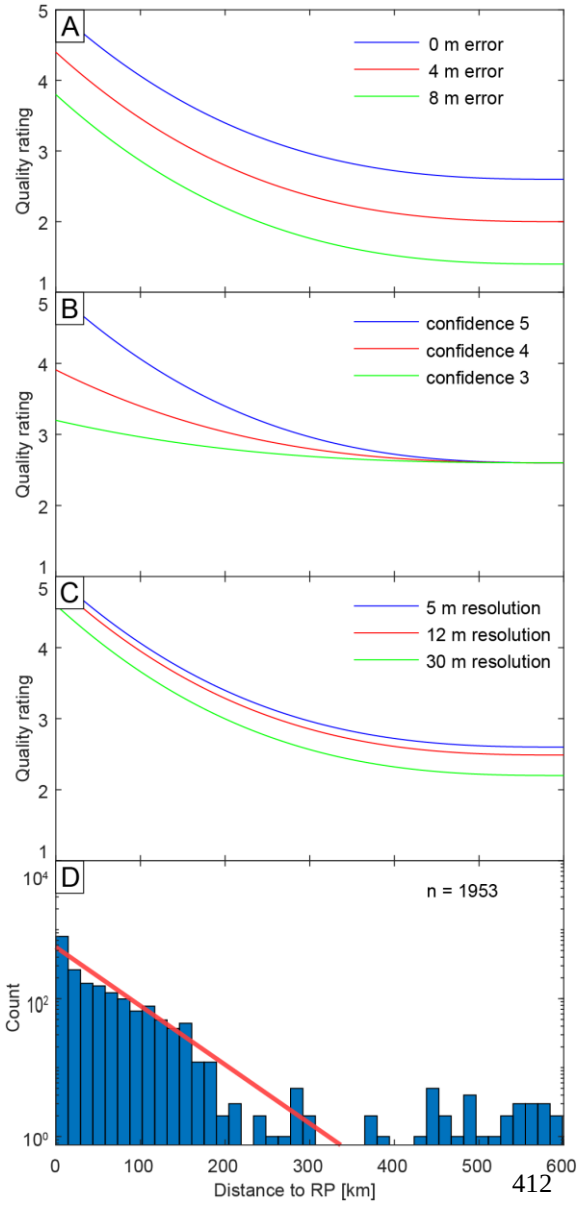

Figure 4. Influence of the parameters on the quality rating. The x-axis is the distance to reference point (RP), the y-axis is the quality rating, the color lines represent different values of quality rating parameters. While one parameter is being tested, the remaining parameters are set to their best values. That is why the QR does not reach values of 1 in the graphs displayed here. (A) Shoreline-angle elevation error. (B) Confidence value of the referencing point. (C) Topographic resolution of the DEM used for terrace-elevation estimation. (D) Histogram displaying the distribution of distances between each shoreline-angle measurement and its nearest RP (n: number of measurements). The red line is an exponential fit.

412

413 ### 3.2. Estimating coastal uplift rates

414 Uplift-rate estimates from marine terraces *(u)* were calculated using equations 2 and 3:

415 **Equation 2: Relative sea level.**

416 $$\Delta H = H_T - H_{SL}$$

417 **Equation 3: Uplift rate.**

418 $$u = \frac{H_T - H_{SL}}{T}$$

where ΔH is the relative sea level, H_{SL} is the sea-level altitude of the interglacial maximum, H_T is the shoreline-angle elevation of the marine terrace, and T its associated age (Lajoie, 1986).

We calculated the standard error $SE(u)$ using equation 4 from Gallen et al. (2014):

Equation 4: Uplift-rate error.

$$SE(u)^2 = u^2\left(\left(\frac{\sigma_{\Delta H}^2}{\Delta H^2}\right) + \left(\frac{\sigma_T^2}{T^2}\right)\right)$$

where $\sigma_{\Delta H}^2$, the error in relative sea level, equals $(\sigma_{H_T}^2 + \sigma_{H_{SL}}^2)$. The standard-error estimates comprise the uncertainty in shoreline-angle elevations from TerraceM (σ_{H_T}), error estimates in absolute sea level $(\sigma_{H_{SL}})$ from Rohling et al. (2009), and an arbitrary range of 10 ka for the duration of the highstand (σ_T).

Vertical displacement rates and relative sea level are influenced by flexural rebound associated with loading and unloading of ice sheets during glacio-isostatic adjustments (GIA) (Stewart et al., 2000; Shepherd and Wingham, 2007). The amplitude and wavelength of GIA is mostly determined by the flexural rigidity of the lithosphere (Turcotte and Schubert, 1982) and should therefore not severely influence vertical deformation along non-glaciated coastal regions (Rabassa and Clapperton, 1990) that are located in the forearc of active subduction zones. This is supported by Creveling et al. (2017) who showed no significant GIA along the WSAC between 1°N and 40°S since MIS-5a. Current GIA models use an oversimplified lithospheric structure defined by horizontal layers of homogeneous rheology (e.g., Creveling et al., 2017), which might be appropriate for cratons and ocean basins, but not necessarily for the forearcs of subduction margins. Therefore, we did not account for the GIA effect on terrace elevations and uplift rates.

3.3. Tectonic parameters of the South American convergent margin

We compared the deformation patterns of marine terraces along the coast of South America with proxies that included crustal faults, bathymetric anomalies, trench-sediment thickness, and distance to the trench. To evaluate the possible control of climatic parameters in the morphology of marine terraces, we compared our data set with wave heights, tidal range, mean annual precipitation rate, and the azimuth of the coastline (Schweller et al., 1981; Bangs and Cande, 1997; von Huene et al., 1997; Collot et al., 2002; Ceccherini et al., 2015; Hayes et al., 2018; Santibáñez et al., 2019; GEBCO Bathymetric Compilation Group, 2020) (Fig. 1).

To evaluate the potential correlations between tectonic parameters and marine terraces, we analyzed the latitudinal variability of these parameters projected along a curved "simple profile" and a 300-km-wide "swath profile" following the trace of the trench. We used simple profiles for visualizing 2D data sets; for instance, to compare crustal faults along the forearc area of the margin (Veloza et al., 2012; Melnick et al., 2020), we projected the seaward tip of each fault. For the trench-sediment thickness, we projected discrete thickness estimates based on measurements from seismic reflection profiles of Bangs and Cande (1997), Collot et al. (2002), Huene et al. (1996), and Schweller et al. (1981). Finally, we projected the discrete trench distances from the point locations of our marine terrace measurements along a simple profile. To compare bathymetric features on the oceanic plate, we used a compilation of bathymetric

measurements at 450 m resolution (GEBCO Bathymetric Compilation Group, 2020). The data set was projected along a curved, 300-km-wide swath profile using TopoToolbox (Schwanghart and Kuhn, 2010).

Finally, to elucidate the influence of climatic factors on marine terrace morphology, we compared the elevation, but also the number of measurements as a proxy for preservation and exposure of marine terraces. We calculated wave heights, tidal ranges, and reference water levels at the point locations of our marine terrace measurements using the Indicative Meaning Calculator (IMCalc) from Lorscheid and Rovere (2019). We used the maximum values of the hourly significant wave height, and for the tidal range we calculated the difference between the highest and lowest astronomical tide. The reference water level represents the averaged position of the paleo sea level with respect to the shoreline-angle elevation and, together with the indicative range (uncertainty), quantifies the indicative meaning (Lorscheid and Rovere, 2019). We furthermore used the high-resolution data set of Ceccherini et al. (2015) for mean annual precipitation, and we compared the azimuth of the coast in order to evaluate its exposure to wind and waves. To facilitate these comparisons, we extracted the values of all these parameters at the point locations of our marine terrace measurements and projected them along a simple profile. Calculations and outputs were processed and elaborated using MATLAB® 2020b.

4. Results

4.1. Marine terrace geomorphology and shoreline-angle elevations

In the following sections we describe our synthesized database of last interglacial marine terrace elevations along the WSAC. Marine terraces of the last interglacial are generally well preserved and almost continuously exposed along the WSAC, allowing the estimation of elevations with a high spatial density. To facilitate the descriptions of marine terrace-elevation patterns, we divided the coastline into four sectors based on their main geomorphic characteristics (Fig. 5): 1) the Talara bend in northern Peru and Ecuador, 2) southern and central Peru, 3) northern Chile, and 4) central and south-central Chile. In total we carried out 1,843 MIS-5e terrace measurements with a median elevation of 30.1 m asl and 110 MIS-5c terrace measurements with a median of 38.6 m. The regions with exceptionally high marine terrace elevations (≥ 100 m) comprise the Manta Peninsula in Ecuador, the San Juan de Marcona area in south-central Peru, and three regions in south-central Chile (Topocalma, Carranza, and Arauco). Marine terraces at high altitudes (≥ 60 m) can also be found in Chile on the Mejillones Peninsula, south of Los Vilos, near Valparaíso, in Tirua, and near Valdivia, while terrace levels only slightly above the median elevation are located at Punta Galera in Ecuador, south of Puerto Flamenco, at Caldera/Bahía Inglesa, near Caleta Chañaral, and near the Quebrada El Moray in the Altos de Talinay area in Chile. In the following sections we describe the characteristics of each site in detail, the names of the sites are written in brackets following the same nomenclature as in the WALIS database (i.e., Pe – Peru, Ec – Ecuador, Ch – Chile).

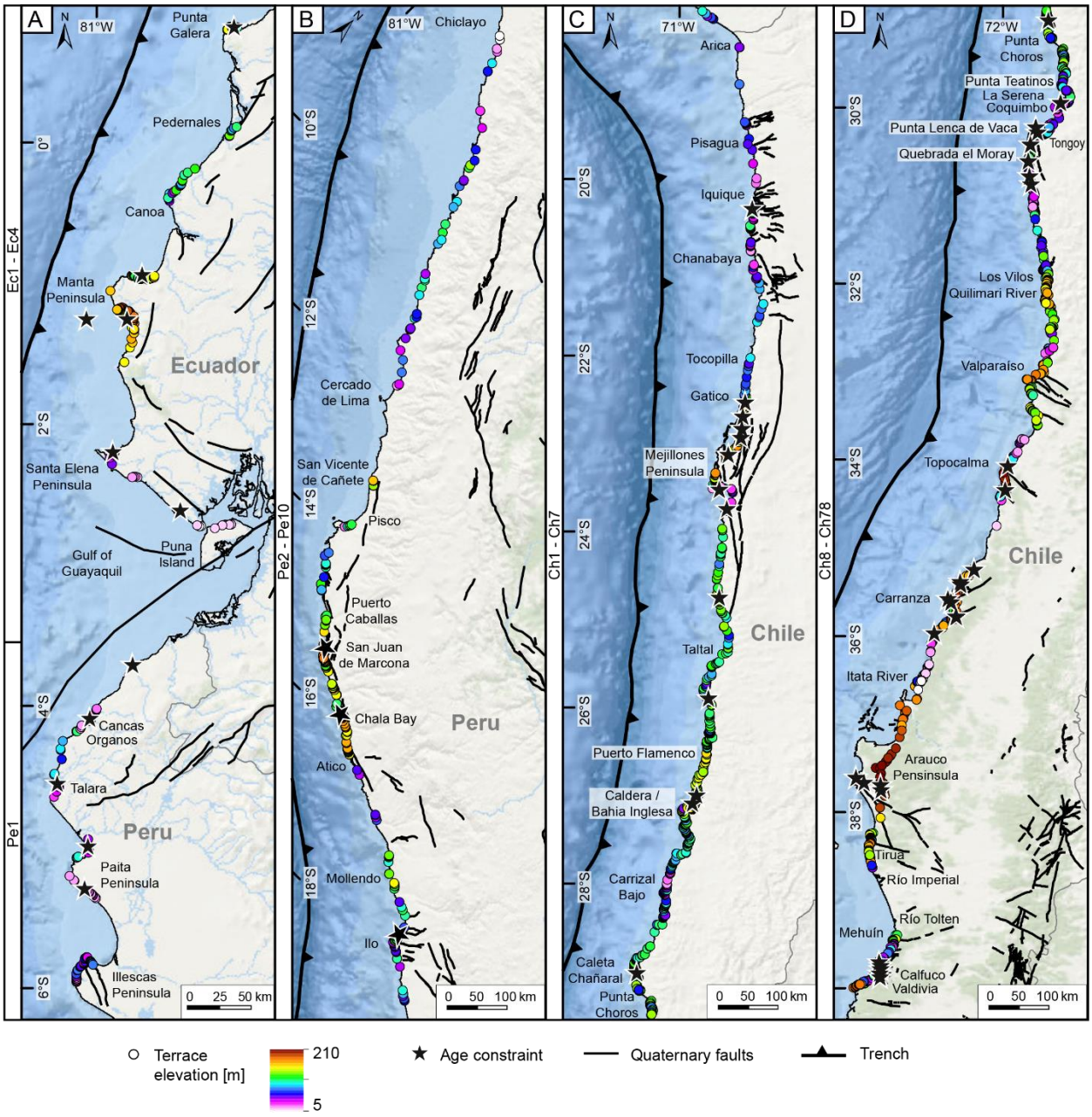

Figure 5. Shoreline-angle elevation measurements (colored points), referencing points (black stars), Quaternary faults (bold black lines) (Veloza et al., 2012; Melnick et al., 2020), and locations mentioned in the text for the four main geomorphic segments (for location see Fig. 1A) (World Ocean Basemap: Esri, Garmin, GEBCO, NOAA NGDC, and other contributors). Site names referring to the entries in the WALIS database are on the left margin of each sub-figure (Pe – Peru, Ec – Ecuador, Ch – Chile). (A) Talara bend in Ecuador and northern Peru. (B) Central and southern Peru. (C) Northern Chile. (D) Central and south-central Chile.

4.1.1. Ecuador and northern Peru (1°N–6.5°S)

The MIS-5e terrace levels in Ecuador and northern Peru [sites Ec1 to Ec4 and Pe1] are discontinuously preserved along the coast (Fig. 6). They often occur at low elevations (between 12 m and 30 m) and show abrupt local changes

in elevation, reaching a maximum at the Manta Peninsula. Punta Galera in northern Ecuador displays relatively broad and well-preserved marine terraces ranging between 40 and 45 m elevation and rapidly decrease eastward to about 30 m asl across the Cumilínche fault [Ec1]. Farther south, between Pedernales and Canoa [Ec1], narrow terraces occur at lower altitudes of 22–34 m asl. A long-wavelength (~120 km) pattern in terrace-elevation change can be observed across the Manta Peninsula with the highest MIS-5e terraces peaking at ~100 m asl at its southern coast [Ec2]. This terrace level is hardly visible in its highest areas with platform widths smaller than 100 m due to deeply incised and narrowly spaced river valleys. We observe lower and variable elevations between 30 and 50 m across the Rio Salado fault in the San Mateo paleo-gulf in the north, while the terrace elevations increase gradually from ~40 m in the Pile paleo-gulf in the south [Ec3] toward the center of the peninsula (El Aromo dome) and the Montecristi fault [Ec3]. A lower terrace level correlated to MIS-5c displays similar elevation patterns as MIS-5e within the Pile paleo-gulf and areas to the north. Near the Gulf of Guayaquil and the Dolores-Guayaquil megashear, the lowest terrace elevations occur at the Santa Elena Peninsula ranging between 17 and 24 m asl and even lower altitudes in its southern part, and on the Puna Island ranging between 11 and 16 m asl [Ec4]. In northern Peru [Pe1], we observe dismembered MIS-5e terraces in the coastal area between Cancas and Talara below the prominent Mancora Tablazo. “Tablazo” is a local descriptive name used in northern Peru (~3.5–6.5°S) for marine terraces that cover a particularly wide surface area (Pedoja et al., 2006b). South of Cancas, MIS-5e terrace elevations range between 17 and 20 m asl, reaching 32 m near Organos, and vary between 20 and 29 m in the vicinity of Talara. In the southward continuation of the Talara harbor, the Talara Tablazo widens, with a lower marine terrace at about 23 m asl immediately north of Paita Peninsula reaching 30 m asl in the northern part of the peninsula. The last occurrence of well-preserved MIS-5e terraces in this sector exists at the Illescas Peninsula, where terrace elevations decrease from around 30 m to 17 m asl southward.

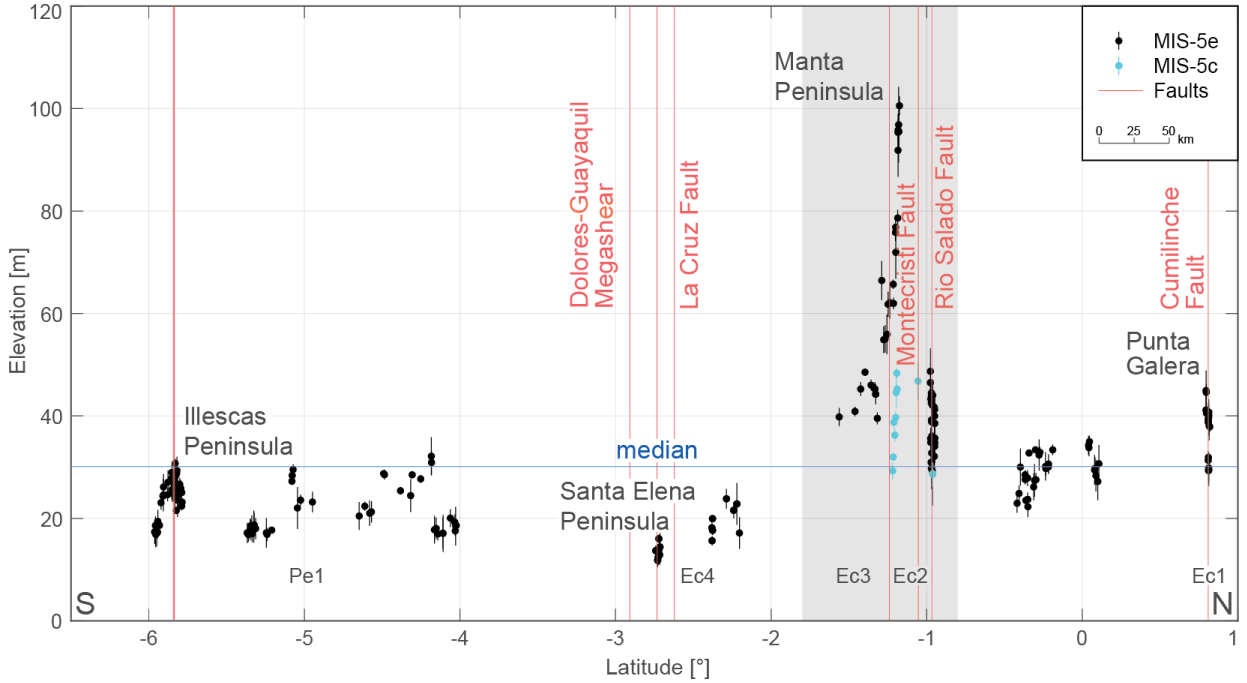

Figure 6. Measured shoreline-angle elevations of MIS-5e and 5c in Ecuador (Ec) and northern Peru (Pe). A high and inferred long-wavelength change in terrace elevation occurs at the Manta Peninsula (gray area) and at low elevations

farther south at the Santa Elena Peninsula. Several terrace-elevation changes over short distances coincide with faulting at Punta Galera and on the Illescas Peninsula. Median elevation: 30.1 m. For location see Fig. 5A.

4.1.2. Central and southern Peru (6.5°–18.3°S)

This segment comprises marine terraces at relatively low and constant elevations, but which are rather discontinuous [sites Pe2 to Pe10], except in the San Juan de Marcona area, where the terraces increase in elevation drastically (Fig. 7). The coast in north-central Peru exhibits poor records of MIS-5e marine terraces, characterized by mostly narrow and discontinuous remnants that are sparsely distributed along the margin with limited age constraints. Marine terraces increase in elevation from 11 to 35 m asl south of Chiclayo [Pe2] and decrease to 17 m asl near Cercado de Lima [Pe3, Pe4], forming a long-wavelength (~600 km), small amplitude (~20 m) upwarped structure. The MIS-5e terrace levels are better expressed in the south-central and southern part of Peru at elevations between 35 and 47 m asl in San Vicente de Cañete, decreasing to approximately 30 m asl in the vicinity of Pisco [Pe5]. South of Pisco, the coastal area becomes narrow with terrace elevations ranging between 25 and 34 m asl [Pe6] and increasing abruptly to 74–79 m near Puerto Caballas and the Río Grande delta. MIS-5e terrace elevations are highest within the San Juan de Marcona area, reaching 109–93 m at Cerro Huevo and 87–56 m at Cerro Trés Hermanas [Pe7]. These higher terrace elevations coincide with a wider coastal area, a better-preserved terrace sequence, and several crustal faults, such as the San Juan and El Huevo faults.

Terrace heights west of Yauca indicate a further decrease to 50–58 m before a renewed increase to 70–72 m can be observed in the Chala embayment [Pe8]. We observe a similar trend in elevation changes for the shoreline angles attributed to the MIS-5c interglacial within the previously described high-elevation area: 31–39 m near the Río Grande delta, 62–58 m below the Cerro Huevo peak, 64–27 m below the Cerro Trés Hermanas peak [Pe7], 36–40 m near Yauca, and 34–40 m within the Chala embayment [Pe8]. Besides various changes in between, terrace elevations decrease slowly from 54 m south of the Chala region to 38 m near Atico [Pe8]. The overall decrease south of the San Juan de Marcona area therefore contrasts strikingly with the sharper decrease to the north. These high-elevation marine terraces, which extend ~250 km along the coast from north of the San Juan de Marcona area to south of Chala Bay, constitute one of the longest wavelength structures of the WSAC. Southeast of Atico, less well-preserved marine terraces appear again in form of small remnants in a narrower coastal area. Starting with elevations as low as 24 m, MIS-5e terrace altitudes increase southeastward to up to 40 m near Mollendo [Pe9], before they slightly decrease again. The broader and quite well-preserved terraces of the adjacent Ilo area resulted in a smooth increase from values greater than 25 m to 33 m and a sudden decrease to as low as 22 m across the Chololo fault [Pe9]. North of the Arica bend, shoreline-angle measurements yielded estimates of 24–29 m in altitude [Pe10].

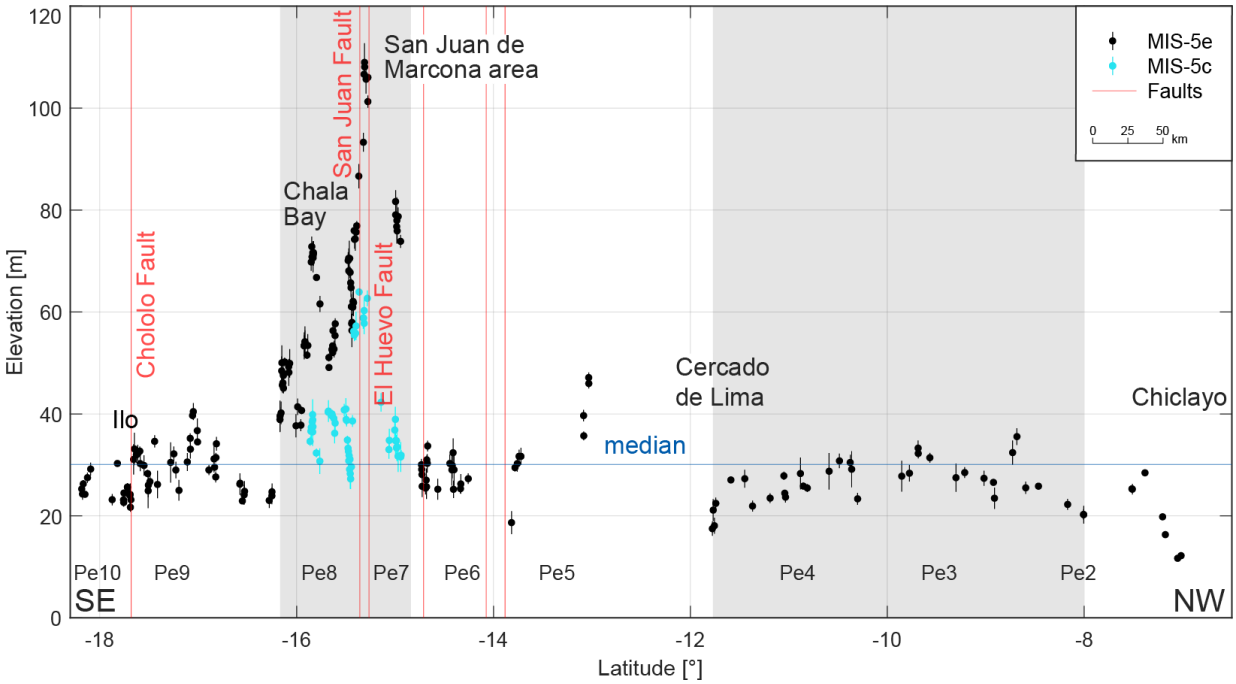

Figure 7. Measured shoreline-angle elevations of MIS-5e and 5c terraces in central and southern Peru (Pe). While only sparsely preserved terraces below the median (30.1 m) occur in central Peru between Chiclayo and Lima, a relatively broad and asymmetric distribution of marine terraces characterizes the area of San Juan de Marcona. For location see Fig. 5B.

4.1.3. Northern Chile (18.3°–29.3°S)

Along the northern Chilean coast, marine terraces of the MIS-5e are characterized by a variable elevation pattern and the occurrence of numerous crustal faults associated with the Atacama fault system, although the changes in terrace elevation are not as pronounced as in the northern segments (Fig. 8) [sites Ch1 to Ch7]. The local widening of the coastal area near the Arica bend narrows southward with MIS-5e terraces at elevations of between 24 and 28 m asl in northernmost Chile [Ch1]. Just north of Pisagua, we measured shoreline-angle elevations of well-preserved marine terraces between 19 and 26 m across the Atajana fault [Ch1]. An areally limited zigzag pattern starting with shoreline-angle elevation values of 32 m south of Iquique and south of the Zofri and Cavancha faults decreases rapidly to approximately 22 m, but increases again to similar altitudes and drops as low as 18 m toward Chanabaya south of the Barranco Alto fault [Ch1]. A gentle, steady rise in terrace elevations can be observed south of Tocopilla where altitudes of 25 m are attained. South of Gatico, terrace markers of the MIS-5e highstand increase and continue northward for much of the Mejillones Peninsula within an approximate elevation range of 32–50 m asl, before reaching a maximum of 62 m asl at the Pampa de Mejillones [Ch2]. With its ~100 km latitudinal extent, we consider this terrace-elevation change to be a medium-wavelength structure. Although no MIS-5e terrace levels have been preserved at the Morro Mejillones Horst (Binnie et al., 2016), we measured shoreline-angle elevations at the elevated southwestern part of the peninsula that decrease sharply from 55 to 17 m asl in the vicinity of the Mejillones fault system [Ch2]. After a short interruption of the MIS-5e terrace level at Pampa Aeropuerto, elevations remain relatively low between 19–25 m farther south [Ch2]. Along the ~300-km coastal stretch south of Mejillones, marine terraces are scattered along the narrow coastal area ranging between 25 and 37 m asl [Ch3]. South of Puerto Flamenco, MIS-5e

terrace elevations range between 40 and 45 m asl until Caldera and Bahía Inglesa [Ch4]. The MIS-5e marine terrace elevations decrease abruptly south of the Caldera fault and the Morro Copiapó (Morro Copiapó fault) to between 25 and 33 m asl, reaching 20 m asl north of Carrizal Bajo [Ch4]. In the southernmost part of the northern Chilean sector, the MIS-5e terraces rise from around 30 m asl to a maximum of 45 m asl near the Cabo Leones fault [Ch4], before decreasing in elevation abruptly near Caleta Chañaral and Punta Choros [Ch5, Ch6, Ch7].

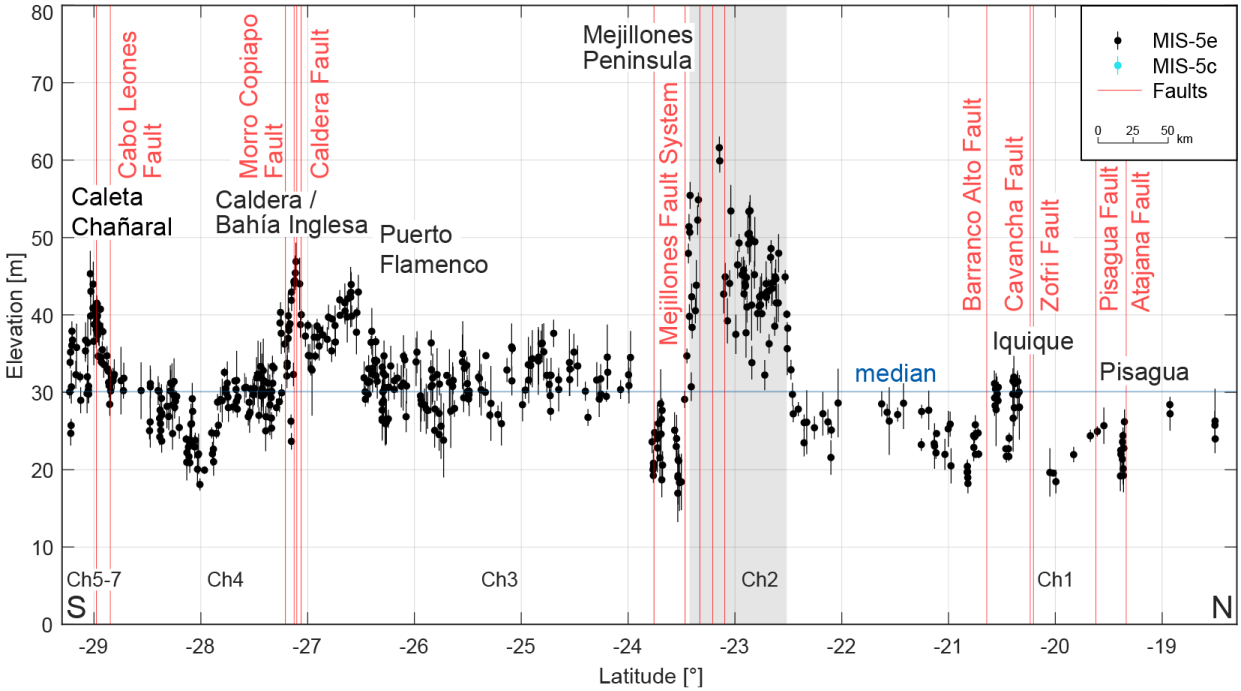

Figure 8. Measured shoreline-angle elevations of MIS-5e and 5c terraces in northern Chile (Ch). Faults and asymmetrically uplifted marine terraces of up to 60 m elevation characterize the Mejillones Peninsula, reaching values below 20 m at the southern margin. Terrace elevations attain peak values south of Puerto Flamenco, at Caldera/Bahía Inglesa, and north of Caleta Chañaral, while in between minimum elevations below 20 m prevail (north of Carizal Bajo). Median elevation is 30.1 m. For location see Fig. 5C.

4.1.4. Central Chile (29.3°–40°S)

Marine terraces along central Chile display variable, high-amplitude terrace-elevation patterns associated with numerous crustal faults, and include a broad-scale change in terrace altitudes with the highest MIS-5e marine terrace elevations of the entire South American margin on the Arauco Peninsula (Fig. 9) [sites Ch8 to Ch78]. South of Punta Choros, marine terrace elevations decrease from values close to 40 to 22 m asl north of Punta Teatinos [Ch8, Ch9]. A maximum elevation of 40 m is reached by the terraces just south of this area [Ch10] whereas north of La Serena, a sharp decrease leads to values between 20 and 30 m for marine terraces south of Coquimbo Bay and in the Tongoy Bay area [Ch11, Ch12]. South of Punta Lengua de Vaca, our measurements of the exceptionally well-preserved staircase morphology of the terraces are within the same elevation range between 20 and 30 m, increasing slowly to 40 m near the Quebrada el Moray [Ch13]. Although we could not observe a significant change in terrace elevation across the Puerto Aldea fault, we measured an offset of ~7 m across the Quebrada Palo Cortado fault. MIS-5e terrace levels decrease thereafter and vary between 20 and 30 m in altitude until north of Los Vilos [Ch14–Ch18], where they increase in elevation [Ch19], reaching 60 m near the Rio Quilimari [Ch20]. The marine terraces become wider in this

area and are associated with scattered sea stacks. Decreasing farther south to only 20 m asl [Ch21–Ch25], the coastal area narrows and has terrace heights of up to 64 m near Valparaíso, in an area that is cut by numerous faults (e.g., Valparaíso and Quintay faults) [Ch26–Ch32]. Another low-elevation area follows southward, with values as low as 17 m [Ch33–Ch35]. Farther south, between 34°S and 38°S, broad (~200 km at Arauco), medium (~45 km at Topocalma), and narrow (Carranza) upwarped zones occur that are manifested by variable terrace elevations. These include prominent high-terrace elevations at Topocalma with a maximum of 180 m [Ch36–Ch39], slightly lower levels of 110 m at Carranza [Ch42–Ch47], exceptionally low values near the Río Itata (< 10 m) [Ch48–Ch64, Ch66], and the most extensive and highest shoreline-angle elevations on the Arauco Peninsula with elevations in excess of 200 m [Ch67–Ch73]. Additionally, we measured MIS-5c terrace elevations in the three higher exposed areas with a range of 20–55 m at Carranzo, and a few locations at Topocalma (76–81 m) and Arauco (117–123 m). The medium-wavelength structure of Topocalma is bounded by the Pichilemu and Topocalma faults, and near Carranza several fault offsets (e.g., Pelluhue and Carranza faults) are responsible for the short-wavelength changes in terrace elevation. In contrast, crustal faulting is nearly absent in the high-elevation and long-wavelength structure at Arauco. MIS-5e terrace elevations are highly variable within a short area south of the Arauco Peninsula near the Tirua fault, increasing rapidly from 27 m to 78 m and decreasing thereafter to approximately 20 m [Ch74, Ch75]. The continuity of terraces is interrupted by the absence of terrace levels between Río Imperial and Río Toltén, but resumes afterward with a highly frequent zigzag pattern and multiple faults (e.g., Estero Ralicura and Curinanco faults) from as low as 18 m to a maximum of 40 m [Ch76, Ch77]. In this area locations with the highest terrace levels comprise the terraces near Mehuín and Calfuco. A final increase in shoreline-angle elevations from about 20–30 m up to 76 m near Valdivia coincides with the southern terminus of our terrace-elevation measurements [Ch78].

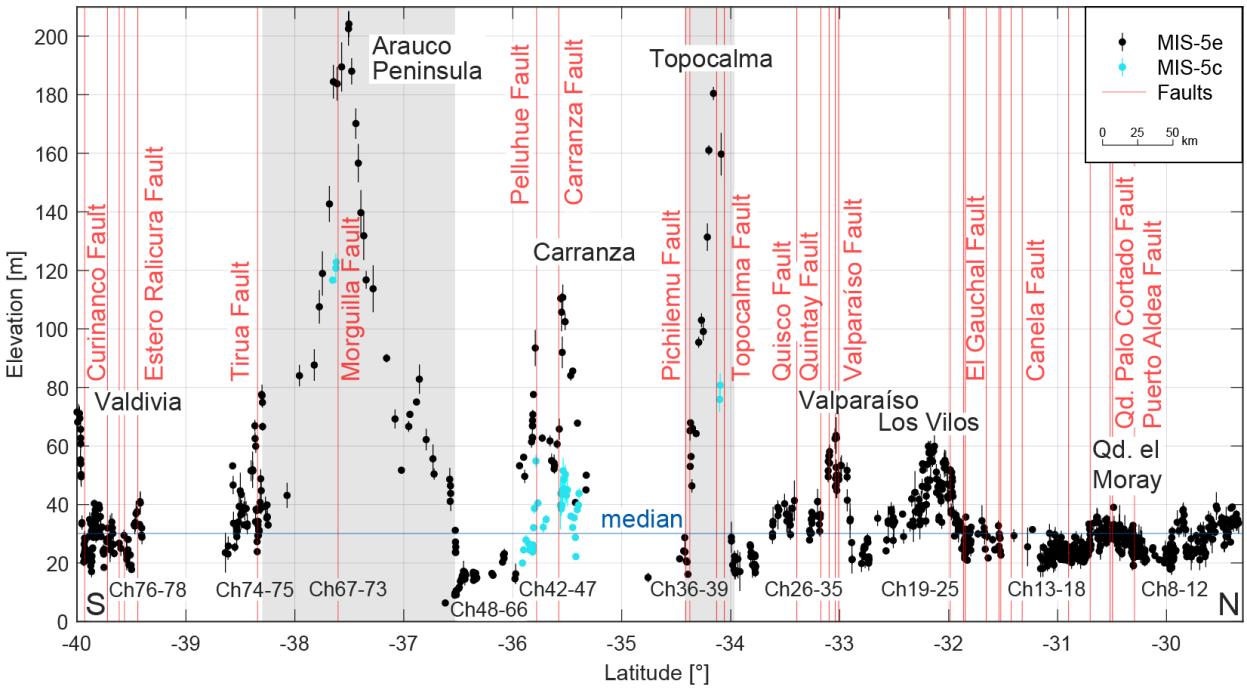

Figure 9. Measured shoreline-angle elevations of MIS-5e and 5c terraces in central Chile (Ch). Extensive faulting coincides with various high terrace elevations of the last interglacial highstand north of Los Vilos, near Valparaiso, at Topocalma, Carranza, and near Valdivia. The most pronounced and long-wavelength change in terrace elevation occurs on the Arauco

Peninsula with maximum elevations over 200 m and minimum elevations below 10 m north of Concepción. Qd. – Quebrada. Median elevation: 30.1 m. For location see Fig. 5D.

4.2. Statistical analysis

Our statistical analysis of mapped shoreline-angle elevations resulted in a maximum kernel density at 28.96 m with a 95% confidence interval from 18.59 m to 67.85 m (2σ) for the MIS-5e terrace level (Fig. 10A). The MIS-5c terrace yielded in a maximum kernel density at a higher elevation of 37.20 m with 2σ ranging from 24.50 m to 63.92 m. It is important to note that the number of MIS-5c measurements is neither as high nor as continuous as compared to that of the MIS-5e level. MIS-5c data points were measured almost exclusively in sites where MIS-5e reach high elevations (e.g., San Juan de Marcona with MIS-5e elevations between 40 and 110 m).

The distribution of measurement errors was studied using probability kernel-density plots for each topographic resolution (1-5 m LIDAR, 12 m TanDEM-X, and 30 m TanDEM-X). The three data sets display similar distributions and maximum likelihood probabilities (MLP); for instance, LiDAR data show a MLP of 0.93 m, the 12 m TanDEM-X a MLP of 1.16 m, and 30 m TanDEM-X a MLP of 0.91 m (Fig. 10B). We observe the lowest errors from the 30 m TanDEM-X, slightly higher errors from the 1-5 m LiDAR data, and the highest errors from the 12 m TanDEM-X. This observation is counterintuitive as we would expect lower errors for topographic data sets with higher resolution (1-5 m LiDAR). The reason for these errors is probably related to the higher number of measurements using the 12 m TanDEM-X (1564) in comparison with the measurements using 30 m TanDEM-X (50), which result in a higher dispersion and a more realistic representation of the measurement errors (Fig. 10B). In addition, the relation between terrace elevations and error estimates shows that comparatively higher errors are associated with higher terrace elevations, although the sparse point density of high terrace-elevation measurements prevents recognition of a clear correlation (Fig. 10C).

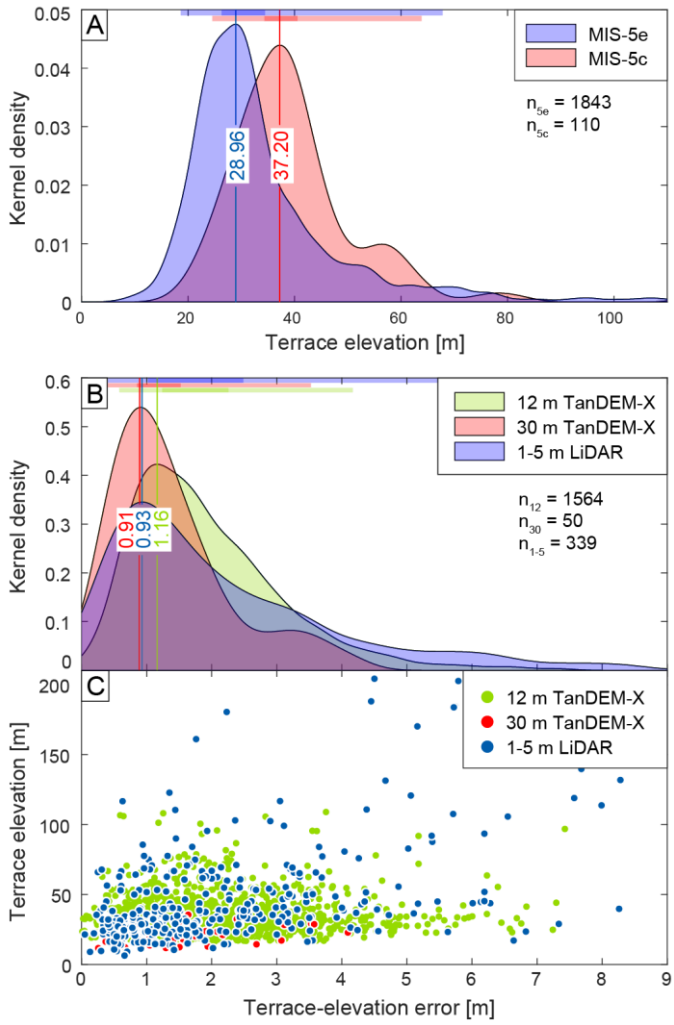

Figure 10. Statistical analysis of measured shoreline-angle elevations. (A) Kernel-density plot of MIS-5e and 5c terrace elevations with maximum likelihood probabilities (m.l.p.) at 28.96 m elevation for MIS-5e and 37.20 m elevation for MIS-5c (n: number of measurements). Colored bars on top highlight the standard deviations σ and 2σ. (B) Kernel-density and their associated standard-deviation (σ and 2σ) calculations of terrace-elevation errors for source DEMs of various resolutions. The most abundant 12 m TanDEM-X has a m.l.p.-error of 1.16 m, while the 30 m TanDEM-X and the 1-5 m LIDAR produce slightly lower errors of 0.91 m and 0.93 m, respectively. (C) Terrace-elevation errors plotted against terrace elevation for the individual source DEMs. Although the point density for high terrace elevations is low, a weak correlation of high errors with high terrace elevations can be observed.

4.3. Coastal uplift-rate estimates

We calculated uplift rates from 1953 terrace-elevation measurements of MIS-5e (1843) and MIS-5c (110) along the WSAC with a median uplift rate of approximately 0.22 m/ka (Fig. 11). As with the distribution of terrace elevations, we similarly observed several small-scale and large-scale, high-amplitude changes in uplift rate along the coast. The most pronounced long-wavelength highs (≥ 1° latitude) in uplift rate are located on the Manta Peninsula (0.79 m/ka), in the San Juan de Marcona area (0.85 m/ka), and on the Arauco Peninsula (1.62 m/ka). Medium-wavelength structures include the Mejillones Peninsula (0.47 m/ka) and Topocalma (1.43 m/ka), while shorter wavelength structures that are characterized by exceptionally high uplift rates seem to be limited to the central Chilean part of the coastline, especially between 31.5° and 40°S. The most striking example includes Carranza with an uplift rate of up to 0.87 m/ka since the formation of the oldest MIS-5 terrace levels. Lower, but still quite high, uplift rates were calculated for areas north of Los Vilos (0.46 m/ka), near Valparaíso (0.49 m/ka), and near Valdivia (0.59 m/ka). The lowest uplift rates along the South American margin occur at Penco immediately north of Concepción (0.03 m/ka), south of Chiclayo in northern Peru (0.07 m/ka), and on the southern Santa Elena Peninsula in Ecuador (0.07 m/ka).

5. Discussion

5.1. Advantages and limitations of the database of last interglacial marine terrace elevations along the WSAC

In this study we generated a systematic database of last interglacial marine terrace elevations with unprecedented resolution based on an almost continuous mapping of ~2,000 measurements along 5,000 km of the WSAC. This opens up several possibilities for future applications in which this database can be used; for example, marine terraces are excellent strain markers that can be used in studies on deformation processes at regional scale, and thus the synthesis allows comparisons between deformation rates at different temporal scales in different sectors of the margin or analyses linking specific climate-driven and tectonic coastal processes, and landscape evolution. However, there are a number of limitations and potential uncertainties that can limit the use of this database in such studies without taking several caveats into consideration.

One of the most critical limitations of using the database is associated with the referencing points used to tie our marine terrace measurements, which are in turn based on the results and chronological constraints provided by previous studies. The referencing points are heterogeneously distributed along the WSAC, resulting in some cases of up to 600 km distance to the nearest constrained point, such as in Central Peru [e.g. Pe2]. This may have a strong influence on the confidence in the measurement of the marine terrace elevation at these sites. In addition, the geochronological control of some of the referencing points may be based on dating methods with pronounced uncertainties (e.g., amino acid racemization, electron spin resonance, terrestrial cosmogenic radionuclides), which may result in equivocal interpretations and chronologies of marine terrace levels. In order to address these potential factors of uncertainty we defined a quality rating (see section 3.1.), which allows classifying our mapping results based on their confidence and reliability. Therefore, by considering measurements above a defined quality it is possible to increase the level of confidence for future studies using this database; however, this might result in a decrease of the number of measurements available for analysis and comparison.

5.2. Tectonic and climatic controls on the elevation and morphology of marine terraces along the WSAC

In this section we provide a brief synthesis of our data set and its implications for coastal processes and overall landscape evolution influenced by a combination of tectonic and climatic forcing factors. This synthesis emphasizes the significance of our comprehensive data set for a variety of coastal research problems that were briefly introduced in section 5.1. Our detailed measurements of marine terraces along the WSAC reveal variable elevations and a heterogeneous distribution of uplift rates associated with patterns of short-, medium-, and long-wavelengths. In addition, we observe different degrees of development of marine terraces along the margin expressed in variable shoreline-angle density. There are several possible causes for this variability, which we explore by comparing terrace-elevation patterns with different climatic and tectonic parameters.

5.2.1. Tectonic controls on coastal uplift rates

683 The spatial distribution of the MIS-5 marine terrace elevations along the convergent South American margin has
684 revealed several high-amplitude and long-wavelength changes with respect to tectonically controlled topography.
685 Long-wavelength patterns in terrace elevation (~10^2 km) are observed at the Manta Peninsula in Ecuador, central Peru
686 between Chiclayo and Lima, San Juan de Marcona (Peru), and on the Arauco Peninsula in Chile, while medium-
687 wavelength structures occur at Mejillones Peninsula and Topocalma (Chile). Instead, short-wavelength patterns in
688 MIS-5 terrace elevations are observed, for instance, near Los Vilos, Valparaíso, and Carranza in Chile.

689 The subduction of bathymetric anomalies has been shown to exert a substantial influence on upper-plate deformation
690 (Fryer and Smoot, 1985; Taylor et al., 1987; Macharé and Ortlieb, 1992; Cloos and Shreve, 1996; Gardner et al., 2013;
691 Wang and Bilek, 2014; Ruh et al., 2016), resulting in temporally and spatially variable fault activity, kinematics, and
692 deformation rates (Mann et al., 1998; Saillard et al., 2011; Morgan and Bangs, 2017; Melnick et al., 2019). When
693 comparing the uplift pattern of MIS-5 marine terraces and the bathymetry of the oceanic plate, we observe that the
694 two long-wavelength structures in this area, on the Manta Peninsula and at San Juan de Marcona, both coincide with
695 the location of the subducting Nazca and Carnegie ridges, respectively (Fig. 11A and B); this was also previously
696 observed by other authors (Macharé and Ortlieb, 1992; Gutscher et al., 1999; Pedoja et al., 2006a; Saillard et al.,
697 2011). In summary, long-wavelength structures in coastal areas of the upper plate may be associated with deep-seated
698 processes (Melosh and Raefsky, 1980; Watts and Daly, 1981) possibly related to changes in the mechanical behavior
699 of the plate interface. In this context it is interesting that the high uplift rates on the Arauco Peninsula do not correlate
700 with bathymetric anomalies, which may suggest a different deformation mechanism. The scarcity of crustal faults
701 described in the Arauco area rather suggests that shallow structures associated with crustal bending and splay-faults
702 occasionally breaching through the upper crust (Melnick et al., 2012; Jara-Muñoz et al., 2015; Jara-Muñoz et al., 2017;
703 Melnick et al., 2019) may cause long-wavelength warping and uplift there (Fig. 11A).

704 In contrast, small-scale bathymetric anomalies correlate in part with the presence of crustal faults perpendicular to the
705 coastal margin near, for instance, the Juan Fernandez, Taltal, and Copiapó ridges (Fig. 11B); this results in short-
706 wavelength structures and a more localized altitudinal differentiation of uplifted terraces. This emphasizes also the
707 importance of last interglacial marine terraces as strain markers with respect to currently active faults, which might be
708 compared in the future with short-term deformation estimates from GPS or the earthquake catalog. In summary, short-
709 wavelength structures in the coastal realms of western South America may be associated with faults that root at shallow
710 depths within the continental crust (Jara-Muñoz et al., 2015; Jara-Muñoz et al., 2017; Melnick et al., 2019).

711 The thickness of sediment in the trench is an additional controlling factor on forearc architecture that may determine
712 which areas of the continental margin are subjected to subduction erosion or accretion (Hilde, 1983; Cloos and Shreve,
713 1988; Menant et al., 2020). Our data shows that the accretionary part of the WSAC (south of the intersection with the
714 Juan Fernandez Ridge at 32.9°S) displays faster median uplift rates of 0.26 m/ka than in the rest of the WSAC (Fig.
715 11B and C). However, no clear correlation is observed between trench fill, uplift rates, and the different structural
716 patterns in the erosive part of the margin. On the other hand, we observe lower uplift rates for greater distances from
717 the trench at the Arica bend, in central Peru, and in the Gulf of Guayaquil, while higher uplift rates occur in areas
718 closer to the trench, such as near the Nazca and Carnegie ridges and the Mejillones Peninsula.

5.2.2. Climatic controls on the formation and preservation of last interglacial marine terraces

The latitudinal climate differences that characterize the western margin of South America may also control coastal morphology and the generation and preservation of marine terraces (Martinod et al., 2016b). In order to evaluate the influence of climate in the generation and/or degradation of marine terraces, we compared the number of marine terrace measurements, which is a proxy for the degree of marine terrace preservation, and climatically controlled parameters such as wave height, tidal range, coastline orientation, and the amount of precipitation.

The maximum wave height along the WSAC decreases northward from ~8 to ~2 m (see section 3.3, Fig. 11D). Similarly, the tidal range decreases progressively northward from 2 to 1 m between Valdivia and San Juan de Marcona, followed by a rapid increase to 4 m between San Juan de Marcona and the Manta Peninsula. We observe an apparent correlation between the number of measurements and the tidal range in the north, between Illescas and Manta (Fig. 11F). Likewise, the increasing trend in the number of measurements southward matches with the increase in wave height (Fig. 11D). An increase of wave height and tidal range may lead to enhanced erosion and morphologically well-expressed marine terraces (Anderson et al., 1999; Trenhaile, 2002), which is consequently reflected in a higher number of measurements that can be carried out. Furthermore, we observe low values for the reference water level (< 0.7 m) resulting from tide and wave-height estimations in IMCalc (Lorscheid and Rovere, 2019), which are used to correct our shoreline-angle measurements in the WALIS database (see section 3.3.).

The control of wave-erosion processes on the morphological expression of marine terraces may be counteracted by erosional processes such as river incision. We note that the high number of preserved marine terraces between Mejillones and Valparaíso decreases southward, which coincides with a sharp increase in mean annual precipitation from 10 to 1000 mm/yr (Fig. 11E and F) and fluvial dissection. However, in the area with a high number of measurements between the Illescas Peninsula and Manta we observe an opposite correlation: higher rainfall associated with an increase of marine terrace preservation (Fig. 11E). This suggests that the interplay between marine terrace generation and degradation processes apparently buffer each other, resulting in different responses under different climatic conditions and coastal settings.

The greater number of marine terraces between Mejillones and Valparaíso and north of Illescas corresponds with a SSW-NNE orientation of the coastline (azimuth between 200 and 220°). In contrast, NW-SE to N-S oriented coastlines (azimuth between 125 and 180°), such as between the Arica and Huancabamba bends, correlate with a lower number of marine terrace measurements (Fig. 11E and F). This observation appears, however, implausible considering that NW-SE oriented coastlines may be exposed more directly to the erosive effect of storm waves associated with winds approaching from the south. We interpret the orientation of the coastline therefore to be of secondary importance at regional scale for the formation of marine terraces compared to other parameters, such as wave height, tidal range, or rainfall.

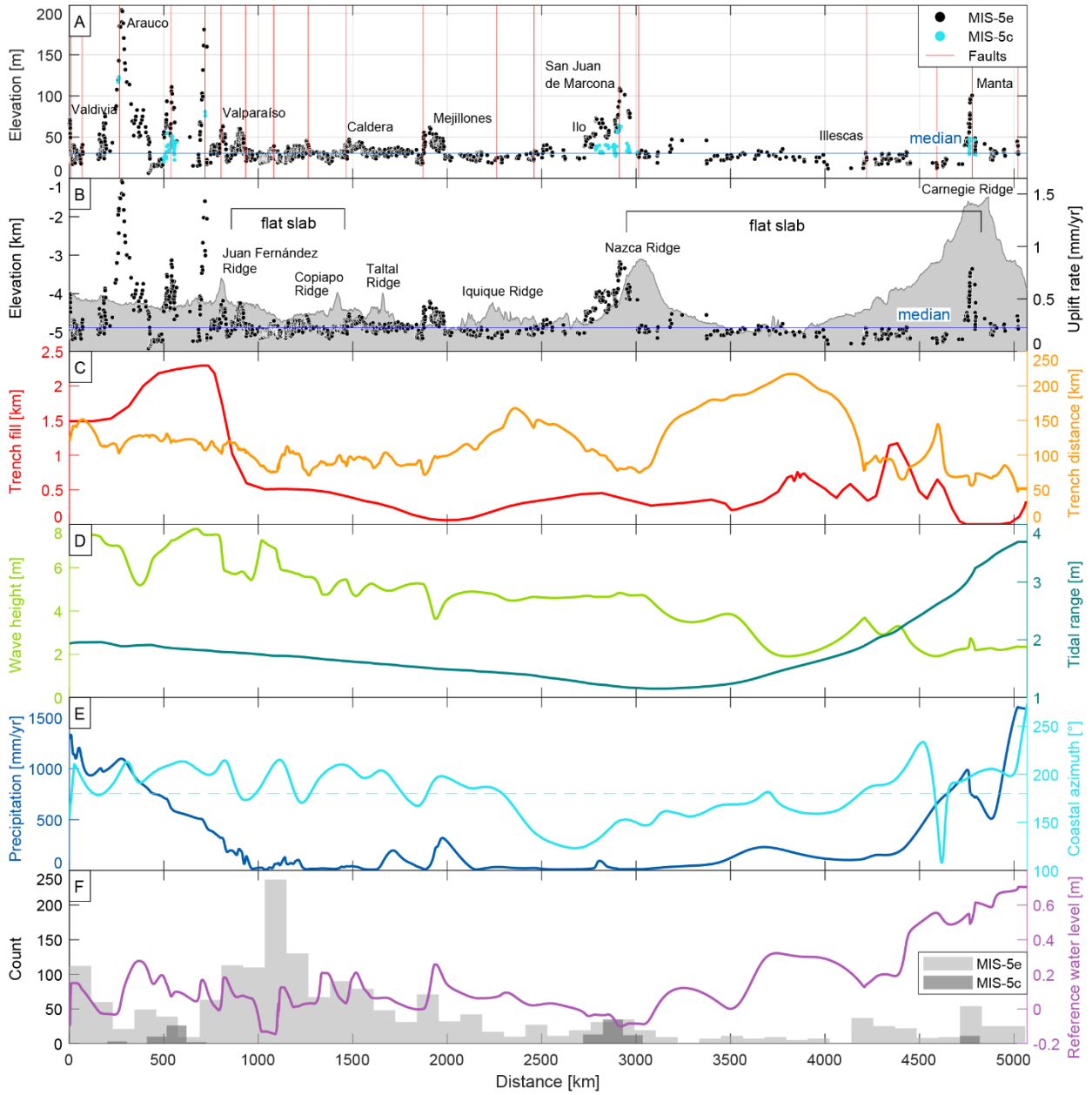

Figure 11. Terrace-elevation and uplift-rate estimates plotted in comparison with various parameters (i.e., bathymetry, trench fill, trench distance, wave height, tidal range, precipitation, and coastal azimuth) that might influence the disparate characteristics of the marine terrace distribution revealed by our data set. We projected these parameters, elevations, and uplift rates with respect to a S-N-oriented polyline that represents the trench. (A) Terrace-elevation measurements and most important crustal faults (Veloza et al., 2012; Melnick et al., 2020). This shows the range of altitudes in different regions along the coast and possible relationships between terrace elevation and crustal faulting. The blue horizontal line indicates the median elevation (30.1 m). (B) Coastal uplift rates and mean bathymetry (GEBCO Bathymetric Compilation Group, 2020) of a 150-km-swath west of the trench. The blue horizontal line indicates the median uplift rate (0.22 mm/a). (C) Sediment thickness of trench-fill deposits (red) (Bangs and Cande, 1997) and the distance of the trench from our terrace measurements (orange). Flat-slab segments of the subducting Nazca plate are indicated for central Chile and Peru. (D) Maximum wave heights along the WSAC (light green) and the tidal range (dark green) between highest and lowest astronomical tides (Lorscheid and Rovere, 2019). (E) Precipitation (blue) along the WSAC (Ceccherini et al., 2015) and azimuthal orientation of the coastline (cyan). (F) Histogram of terrace-elevation measurements along the WSAC.

6. Conclusions

We measured 1,953 shoreline-angle elevations as proxies for paleo-sea levels of the MIS-5e and 5c terraces along ~5,000 km of the WSAC between Ecuador and Southern Chile. Our measurements are based on a systematic methodology and the resulting data have been standardized within the framework of the WALIS database. Our mapping was tied using referencing points based on previously published terrace-elevation estimates and age constraints that are summarized in the compilation of Pedoja et al. (2011). The limitations of this database are associated with the temporal accuracy and spatial distribution of the referencing points, which we attempt to consider by providing a quality-rating value to each measurement. The marine terrace elevations display a median value of 30.1 m for the MIS-5e level and a median uplift rate of 0.22 m/ka for MIS-5e and 5c. The lowest terrace elevations and uplift rates along the entire WSAC occur immediately north of Concepción in Chile (6 m, 0.03 m/ka), south of Chiclayo in northern Peru, and on the Santa Elena Peninsula in Ecuador (both 12 m, 0.07 m/ka). The regions with exceptionally high marine terrace elevations (≥ 100 m) comprise the Manta Peninsula in Ecuador, the San Juan de Marcona area in south-central Peru, and three regions in south-central Chile (Topocalma, Carranza, and Arauco).

The pattern of terrace elevations displays short-, medium- and long-wavelength structures controlled by a combination of various mechanisms. Long-wavelength structures may be controlled by deep-seated processes at the plate interface, such as the subduction of major bathymetric anomalies (e.g. Manta Peninsula and San Juan de Marcona region). In contrast, short- and medium-wavelength deformation patterns may be controlled by crustal faults rooted within the upper plate (e.g., between Mejillones and Valparaíso).

Latitudinal climate characteristics along the WSAC may influence the generation and preservation of marine terraces. An increase in wave height and tidal range generally results in enhanced erosion and morphologically well-expressed, sharply defined marine terraces, which correlates with the southward increase in the number of our marine terrace measurements. Conversely, river incision and lateral scouring in areas with high precipitation may degrade marine terraces, thus decreasing the number of potential marine terrace measurements, such as observed south of Valparaíso.

Data availability. The South American database of last interglacial shoreline-angle elevations is available online at http://doi.org/10.5281/zenodo.4309748 (Freisleben et al., 2020). The description of the WALIS-database fields can be found at https://doi.org/10.5281/zenodo.3961543 (Rovere et al., 2020).

Author contributions. The main compilers of the database were R.F., J.M.M., and J.J. The paper was written by R.F. with significant input from J.J., D.M., M.S. regarding interpretation and further improvements of graphical data representation.

Acknowledgments. We thank Alessio Rovere for his assistance with the WALIS database. The WALIS database was developed by the ERC Starting Grant “Warmcoasts" (ERC-StG-802414) and PALSEA. PALSEA is a working group of the International Union for Quaternary Sciences (INQUA) and Past Global Changes (PAGES), which in turn received support from the Swiss Academy of Sciences and the Chinese Academy of Sciences. The structure of the database was designed by A. Rovere, D. Ryan, T. Lorscheid, A. Dutton, P. Chutcharavan, D. Brill, N. Jankowski, D. Mueller, M. Bartz, E.J. Gowan and K. Cohen. This study was supported by the Millennium Scientific Initiative of the Chilean government through grant NC160025 “Millennium Nucleus CYCLO The Seismic Cycle Along Subduction Zones”, Chilean National Fund for Development of Science and Technology (FONDECYT) grants 1181479 and 1190258, the ANID PIA Anillo ACT192169. R.F. was supported by a research grant of Deutsche

Forschungsgemeinschaft to M.S. (DFG STR373/41-1). Constructive reviews by V. Regard and P.M. Figueiredo helped to improve the paper.

7. References

Anderson, R.S., Densmore, A.L., Ellis, M.A., 1999. The generation and degradation of marine terraces. Basin Research 11(1), 7–19. doi:10.1046/j.1365-2117.1999.00085.x.

Angermann, D., Klotz, J., Reigber, C., 1999. Space-geodetic estimation of the Nazca-South America Euler vector. Earth and Planetary Science Letters 171(3), 329–334. doi:10.1016/S0012-821X(99)00173-9.

Baker, A., Allmendinger, R.W., Owen, L.A., Rech, J.A., 2013. Permanent deformation caused by subduction earthquakes in northern Chile. Nature Geoscience 6(6), 492–496. doi:10.1038/ngeo1789.

Bangs, N.L., Cande, S.C., 1997. Episodic development of a convergent margin inferred from structures and processes along the southern Chile margin. Tectonics 16(3), 489–503.

Barazangi, M., Isacks, B.L., 1976. Spatial distribution of earthquakes and subduction of the Nazca plate beneath South America. Geology 4(11), 686. doi:10.1130/0091-7613(1976)4<686:SDOEAS>2.0.CO;2.

Beck, S., Barrientos, S., Kausel, E., Reyes, M., 1998. Source characteristics of historic earthquakes along the central Chile subduction zone. Journal of South American Earth Sciences 11(2), 115–129. doi:10.1016/S0895-9811(98)00005-4.

Bendix, J., Rollenbeck, R., Reudenbach, C., 2006. Diurnal patterns of rainfall in a tropical Andean valley of southern Ecuador as seen by a vertically pointing K-band Doppler radar. International Journal of Climatology 26(6), 829–846. doi:10.1002/joc.1267.

Bernhardt, A., Hebbeln, D., Regenberg, M., Lückge, A., Strecker, M.R., 2016. Shelfal sediment transport by an undercurrent forces turbidity-current activity during high sea level along the Chile continental margin. Geology 44(4), 295–298. doi:10.1130/G37594.1.

Bernhardt, A., Schwanghart, W., Hebbeln, D., Stuut, J.-B.W., Strecker, M.R., 2017. Immediate propagation of deglacial environmental change to deep-marine turbidite systems along the Chile convergent margin. Earth and Planetary Science Letters 473, 190–204. doi:10.1016/j.epsl.2017.05.017.

Bilek, S.L., 2010. Invited review paper: Seismicity along the South American subduction zone: Review of large earthquakes, tsunamis, and subduction zone complexity. Tectonophysics 495(1-2), 2–14. doi:10.1016/j.tecto.2009.02.037.

Bilek, S.L., Schwartz, S.Y., DeShon, H.R., 2003. Control of seafloor roughness on earthquake rupture behavior. Tectonics 31(5), 455. doi:10.1130/0091-7613(2003)031<0455:COSROE>2.0.CO;2.

837 Binnie, A., Dunai, T.J., Binnie, S.A., Victor, P., González, G., Bolten, A., 2016. Accelerated late quaternary uplift
838 revealed by 10Be exposure dating of marine terraces, Mejillones Peninsula, northern Chile. Quaternary
839 Geochronology 36, 12–27. doi:10.1016/j.quageo.2016.06.005.

840 Bookhagen, B., Strecker, M.R., 2008. Orographic barriers, high-resolution TRMM rainfall, and relief variations
841 along the eastern Andes. Geophysical Research Letters 35(6), 139. doi:10.1029/2007GL032011.

842 Cahill, T., Isacks, B.L., 1992. Seismicity and shape of the subducted Nazca Plate. Journal of Geophysical Research
843 97(B12), 17503. doi:10.1029/92JB00493.

844 Ceccherini, G., Ameztoy, I., Hernández, C., Moreno, C., 2015. High-Resolution Precipitation Datasets in South
845 America and West Africa based on Satellite-Derived Rainfall, Enhanced Vegetation Index and Digital Elevation
846 Model. Remote Sensing 7(5), 6454–6488. doi:10.3390/rs70506454.

847 Cembrano, J., Lavenu, A., Yañez, G., Riquelme, R., García, M., González, G., Hérail, G., 2007. Neotectonics. In:
848 Moreno, T., Gibbons, W. (Eds.), The geology of Chile. Geological Society, London, pp. 231–261.

849 Clift, P., Vannucchi, P., 2004. Controls on tectonic accretion versus erosion in subduction zones: Implications for
850 the origin and recycling of the continental crust. Reviews of Geophysics 42(2), 19. doi:10.1029/2003RG000127.

851 Clift, P.D., Hartley, A.J., 2007. Slow rates of subduction erosion and coastal underplating along the Andean margin
852 of Chile and Peru. Geology 35(6), 503. doi:10.1130/G23584A.1.

853 Cloos, M., Shreve, R.L., 1988. Subduction-channel model of prism accretion, melange formation, sediment
854 subduction, and subduction erosion at convergent plate margins: 1. Background and description. Pure and
855 Applied Geophysics 128(3-4), 455–500. doi:10.1007/BF00874548.

856 Cloos, M., Shreve, R.L., 1996. Shear-zone thickness and the seismicity of Chilean- and Marianas-type subduction
857 zones. Geology 24(2), 107. doi:10.1130/0091-7613(1996)024<0107:SZTATS>2.3.CO;2.

858 Collot, J.-Y., Charvis, P., Gutscher, M.-A., Operto, S., 2002. Exploring the Ecuador-Colombia Active Margin and
859 Interplate Seismogenic Zone. Eos, Transactions, American Geophysical Union 83(17), 185.
860 doi:10.1029/2002EO000120.

861 Collot, J.-Y., Sanclemente, E., Nocquet, J.-M., Leprêtre, A., Ribodetti, A., Jarrin, P., Chlieh, M., Graindorge, D.,
862 Charvis, P., 2017. Subducted oceanic relief locks the shallow megathrust in central Ecuador. Journal of
863 Geophysical Research: Solid Earth 122(5), 3286–3305. doi:10.1002/2016JB013849.

864 Costa, C., Alvarado, A., Audemard, F., Audin, L., Benavente, C., Bezerra, F.H., Cembrano, J., González, G., López,
865 M., Minaya, E., Santibañez, I., Garcia, J., Arcila, M., Pagani, M., Pérez, I., Delgado, F., Paolini, M., Garro, H.,
866 2020. Hazardous faults of South America; compilation and overview. Journal of South American Earth Sciences
867 104(1), 102837. doi:10.1016/j.jsames.2020.102837.

868 Costa, C., Machette, M.N., Dart, R.L., Bastias, H.E., Paredes, J.D., Perucca, L.P., Tello, G.E., Haller, K.M., 2000.
869 Map and database of Quaternary faults and folds in Argentina. Open-File Report. US Geological Survey.
870 http://dx.doi.org/10.3133/ofr00108.

871 Coudurier-Curveur, A., Lacassin, R., Armijo, R., 2015. Andean growth and monsoon winds drive landscape
872 evolution at SW margin of South America. Earth and Planetary Science Letters 414, 87–99.
873 doi:10.1016/j.epsl.2014.12.047.

874 Creveling, J.R., Mitrovica, J.X., Clark, P.U., Waelbroeck, C., Pico, T., 2017. Predicted bounds on peak global mean
875 sea level during marine isotope stages 5a and 5c. Quaternary Science Reviews 163(6), 193–208.
876 doi:10.1016/j.quascirev.2017.03.003.

877 DeMets, C., Gordon, R.G., Argus, D.F., 2010. Geologically current plate motions. Geophysical Journal International
878 181(1), 1–80. doi:10.1111/j.1365-246X.2009.04491.x.

879 Espurt, N., Funiciello, F., Martinod, J., Guillaume, B., Regard, V., Faccenna, C., Brusset, S., 2008. Flat subduction
880 dynamics and deformation of the South American plate: Insights from analog modeling. Tectonics 27(3), n/a-
881 n/a. doi:10.1029/2007TC002175.

882 Freisleben, R., Jara-Muñoz, J., Melnick, D., Martínez, J.M., Strecker, M., 2020. Marine terraces of the last
883 interglacial period along the Pacific coast of South America (1°N-40°S). Zenodo.
884 doi:10.5281/ZENODO.4309748.

885 Fryer, P., Smoot, N.C., 1985. Processes of seamount subduction in the Mariana and Izu-Bonin trenches. Marine
886 Geology 64(1-2), 77–90. doi:10.1016/0025-3227(85)90161-6.

887 Fuenzalida, H., Cooke, R., Paskoff, R., Segerstrom, K., Weischet, W., 1965. High Stands of Quaternary Sea Level
888 Along the Chilean Coast. Geological Society of America Special Papers 84, 473–496.

889 Gallen, S.F., Wegmann, K.W., Bohnenstiehl, D.R., Pazzaglia, F.J., Brandon, M.T., Fassoulas, C., 2014. Active
890 simultaneous uplift and margin-normal extension in a forearc high, Crete, Greece. Earth and Planetary Science
891 Letters 398, 11–24. doi:10.1016/j.epsl.2014.04.038.

892 Gardner, T.W., Fisher, D.M., Morell, K.D., Cupper, M.L., 2013. Upper-plate deformation in response to flat slab
893 subduction inboard of the aseismic Cocos Ridge, Osa Peninsula, Costa Rica. Lithosphere 5(3), 247–264.
894 doi:10.1130/L251.1.

895 Garreaud, R.D., 2009. The Andes climate and weather. Advances in Geosciences 22, 3–11. doi:10.5194/adgeo-22-3-
896 2009.

897 GEBCO Bathymetric Compilation Group, 2020. The GEBCO_2020 Grid - a continuous terrain model of the global
898 oceans and land. British Oceanographic Data Centre, National Oceanography Centre, NERC, UK.

Geersen, J., Ranero, C.R., Barckhausen, U., Reichert, C., 2015. Subducting seamounts control interplate coupling and seismic rupture in the 2014 Iquique earthquake area. Nature communications 6, 8267. doi:10.1038/ncomms9267.

German Aerospace Center (DLR), 2018. TanDEM-X - Digital Elevation Model (DEM) - Global, 12m.

González, G., Carrizo, D., 2003. Segmentación, cinemática y cronología relativa de la deformación tardía de la Falla Salar del Carmen, Sistema de Fallas de Atacama, (23°40'S), norte de Chile. Revista Geológica de Chile 30(2). doi:10.4067/S0716-02082003000200005.

Goy, J.L., Macharé, J., Ortlieb, L., Zazo, C., 1992. Quaternary shorelines in Southern Peru a record of global sea-level fluctuations and tectonic uplift in Chala Bay. Quaternary International 15-16, 99–112.

Gutscher, M.-A., Malavieille, J., Lallemand, S., Collot, J.-Y., 1999. Tectonic segmentation of the North Andean margin: impact of the Carnegie Ridge collision. Earth and Planetary Science Letters 168(3-4), 255–270. doi:10.1016/S0012-821X(99)00060-6.

Gutscher, M.-A., Spakman, W., Bijwaard, H., Engdahl, E.R., 2000. Geodynamics of flat subduction: Seismicity and tomographic constraints from the Andean margin. Tectonics 19(5), 814–833. doi:10.1029/1999TC001152.

Hampel, A., 2002. The migration history of the Nazca Ridge along the Peruvian active margin: a re-evaluation. Earth and Planetary Science Letters 203(2), 665–679. doi:10.1016/S0012-821X(02)00859-2.

Hayes, G.P., Moore, G.L., Portner, D.E., Hearne, M., Flamme, H., Furtney, M., Smoczyk, G.M., 2018. Slab2, a comprehensive subduction zone geometry model. Science (New York, N.Y.) 362(6410), 58–61. doi:10.1126/science.aat4723.

Hearty, P.J., Hollin, J.T., Neumann, A.C., O'Leary, M.J., McCulloch, M., 2007. Global sea-level fluctuations during the Last Interglaciation (MIS 5e). Quaternary Science Reviews 26(17-18), 2090–2112. doi:10.1016/j.quascirev.2007.06.019.

Hilde, T.W.C., 1983. Sediment subduction versus accretion around the pacific. Tectonophysics 99(2-4), 381–397. doi:10.1016/0040-1951(83)90114-2.

Houston, J., Hartley, A.J., 2003. The central Andean west-slope rainshadow and its potential contribution to the origin of hyper-aridity in the Atacama Desert. International Journal of Climatology 23(12), 1453–1464. doi:10.1002/joc.938.

Hsu, J.T., 1992. Quaternary uplift of the Peruvian coast related to the subduction of the Nazca Ridge: 13.5 to 15.6 degrees south latitude. Quaternary International 15-16, 87–97. doi:10.1016/1040-6182(92)90038-4.

Hsu, J.T., Leonard, E.M., Wehmiller, J.F., 1989. Aminostratigraphy of Peruvian and Chilean Quaternary marine terraces. Quaternary Science Reviews 8(3), 255–262. doi:10.1016/0277-3791(89)90040-1.

930 Huene, R. von, Pecher, I.A., Gutscher, M.-A., 1996. Development of the accretionary prism along Peru and material
931 flux after subduction of Nazca Ridge. Tectonics 15(1), 19–33. doi:10.1029/95TC02618.

932 Jaillard, E., Hérail, G., Monfret, T., Díaz-Martínez, E., Baby, P., Lavenu, A., Dumont, J.F., 2000. Tectonic evolution
933 of the Andes of Ecuador, Peru, Bolivia, and northernmost Chile. In: Cordani, U.G., Milani, E.J., Thomaz, F.A.,
934 Campos, D.A. (Eds.), Tectonic evolution of South America. Sociedad Brasileira de Geologia, Rio de Janeiro,
935 pp. 481–559.

936 Jara-Muñoz, J., Melnick, D., Brill, D., Strecker, M.R., 2015. Segmentation of the 2010 Maule Chile earthquake
937 rupture from a joint analysis of uplifted marine terraces and seismic-cycle deformation patterns. Quaternary
938 Science Reviews 113, 171–192. doi:10.1016/j.quascirev.2015.01.005.

939 Jara-Muñoz, J., Melnick, D., Socquet, A., Cortés-Aranda, J., Strecker, M.R., 2018. Slip rate and earthquake
940 recurrence of the Pichilemu Fault. Congreso Geológico Chileno, 15th.

941 Jara-Muñoz, J., Melnick, D., Strecker, M.R., 2016. TerraceM: A MATLAB® tool to analyze marine and lacustrine
942 terraces using high-resolution topography. Geosphere 12(1), 176–195. doi:10.1130/GES01208.1.

943 Jara-Muñoz, J., Melnick, D., Zambrano, P., Rietbrock, A., González, J., Argandoña, B., Strecker, M.R., 2017.
944 Quantifying offshore fore-arc deformation and splay-fault slip using drowned Pleistocene shorelines, Arauco
945 Bay, Chile. Journal of Geophysical Research: Solid Earth 122(6), 4529–4558. doi:10.1002/2016JB013339.

946 Jordan, T.E., Isacks, B.L., Allmendinger, R.W., Brewer, J.A.O.N., Ramos, V.A., Ando, C.J., 1983. Andean tectonics
947 related to geometry of subducted Nazca plate. Geological Society of America Bulletin 94(3), 341.
948 doi:10.1130/0016-7606(1983)94<341:ATRTGO>2.0.CO;2.

949 Kay, S.M., Maksaev, V., Moscoso, R., Mpodozis, C., Nasi, C., 1987. Probing the evolving Andean Lithosphere:
950 Mid-Late Tertiary magmatism in Chile (29°–30°30′S) over the modern zone of subhorizontal subduction.
951 Journal of Geophysical Research 92(B7), 6173. doi:10.1029/JB092iB07p06173.

952 Lajoie, K.R., 1986. Coastal tectonics. In: Wallace, R.E. (Ed.), Active tectonics. National Academics Press,
953 Washington D.C., pp. 95–124.

954 Lamb, S., Davis, P., 2003. Cenozoic climate change as a possible cause for the rise of the Andes. Nature 425(6960),
955 792–797. doi:10.1038/nature02049.

956 Lohrmann, J., Kukowski, N., Adam, J., Oncken, O., 2003. The impact of analogue material properties on the
957 geometry, kinematics, and dynamics of convergent sand wedges. Journal of Structural Geology 25(10), 1691–
958 1711. doi:10.1016/S0191-8141(03)00005-1.

959 Lorscheid, T., Rovere, A., 2019. The indicative meaning calculator – quantification of paleo sea-level relationships
960 by using global wave and tide datasets. Open Geospatial Data, Software and Standards 4(1), 591.
961 doi:10.1186/s40965-019-0069-8.

962 Macharé, J., Ortlieb, L., 1992. Plio-Quaternary vertical motions and the subduction of the Nazca Ridge, central coast
963 of Peru. Tectonophysics 205(1-3), 97–108. doi:10.1016/0040-1951(92)90420-B.

964 Maldonado, V., Contreras, M., Melnick, D., 2021. A comprehensive database of active and potentially-active
965 continental faults in Chile at 1:25,000 scale. Scientific data 8(1), 20. doi:10.1038/s41597-021-00802-4.

966 Manea, V.C., Pérez-Gussinyé, M., Manea, M., 2012. Chilean flat slab subduction controlled by overriding plate
967 thickness and trench rollback. Geology 40(1), 35–38. doi:10.1130/G32543.1.

968 Mann, P., Taylor, F.W., Lagoe, M.B., Quarles, A., Burr, G., 1998. Accelerating late Quaternary uplift of the New
969 Georgia Island Group (Solomon island arc) in response to subduction of the recently active Woodlark spreading
970 center and Coleman seamount. Tectonophysics 295(3-4), 259–306. doi:10.1016/S0040-1951(98)00129-2.

971 Marcaillou, B., Collot, J.-Y., Ribodetti, A., d'Acremont, E., Mahamat, A.-A., Alvarado, A., 2016. Seamount
972 subduction at the North-Ecuadorian convergent margin: Effects on structures, inter-seismic coupling and
973 seismogenesis. Earth and Planetary Science Letters 433, 146–158. doi:10.1016/j.epsl.2015.10.043.

974 Martinod, J., Regard, V., Letourmy, Y., Henry, H., Hassani, R., Baratchart, S., Carretier, S., 2016a. How do
975 subduction processes contribute to forearc Andean uplift? Insights from numerical models. Journal of
976 Geodynamics 96, 6–18. doi:10.1016/j.jog.2015.04.001.

977 Martinod, J., Regard, V., Riquelme, R., Aguilar, G., Guillaume, B., Carretier, S., Cortés-Aranda, J., Leanni, L.,
978 Hérail, G., 2016b. Pleistocene uplift, climate and morphological segmentation of the Northern Chile coasts
979 (24°S–32°S): Insights from cosmogenic 10Be dating of paleoshorelines. Geomorphology 274, 78–91.
980 doi:10.1016/j.geomorph.2016.09.010.

981 Melet, A., Teatini, P., Le Cozannet, G., Jamet, C., Conversi, A., Benveniste, J., Almar, R., 2020. Earth Observations
982 for Monitoring Marine Coastal Hazards and Their Drivers. Surveys in Geophysics 41(6), 1489–1534.
983 doi:10.1007/s10712-020-09594-5.

984 Melnick, D., 2016. Rise of the central Andean coast by earthquakes straddling the Moho. Nature Geoscience 9(5),
985 401–407. doi:10.1038/ngeo2683.

986 Melnick, D., Bookhagen, B., Echtler, H.P., Strecker, M.R., 2006. Coastal deformation and great subduction
987 earthquakes, Isla Santa Maria, Chile (37°S). Geological Society of America Bulletin 118(11-12), 1463–1480.
988 doi:10.1130/B25865.1.

989 Melnick, D., Bookhagen, B., Strecker, M.R., Echtler, H.P., 2009. Segmentation of megathrust rupture zones from
990 fore-arc deformation patterns over hundreds to millions of years, Arauco peninsula, Chile. Journal of
991 Geophysical Research: Solid Earth 114(B1), 6140. doi:10.1029/2008JB005788.

992 Melnick, D., Hillemann, C., Jara-Muñoz, J., Garrett, E., Cortés-Aranda, J., Molina, D., Tassara, A., Strecker, M.R.,
993 2019. Hidden Holocene slip along the coastal El Yolki Fault in Central Chile and its possible link with

megathrust earthquakes. Journal of Geophysical Research: Solid Earth 124(7), 7280–7302. doi:10.1029/2018JB017188.

Melnick, D., Maldonado, V., Contreras, M., 2020. Database of active and potentially-active continental faults in Chile at 1:25,000 scale. PANGAEA - Data Publisher for Earth & Environmental Science. doi:10.1594/PANGAEA.922241.

Melosh, H.J., Raefsky, A., 1980. The dynamical origin of subduction zone topography. Geophysical Journal International 60(3), 333–354. doi:10.1111/j.1365-246X.1980.tb04812.x.

Menant, A., Angiboust, S., Gerya, T., Lacassin, R., Simoes, M., Grandin, R., 2020. Transient stripping of subducting slabs controls periodic forearc uplift. Nature communications 11(1), 1823. doi:10.1038/s41467-020-15580-7.

Morgan, J.K., Bangs, N.L., 2017. Recognizing seamount-forearc collisions at accretionary margins: Insights from discrete numerical simulations. Geology 45(7), 635–638. doi:10.1130/G38923.1.

Müller, R.D., Sdrolias, M., Gaina, C., Roest, W.R., 2008. Age, spreading rates, and spreading asymmetry of the world's ocean crust. Geochemistry, Geophysics, Geosystems 9(4). doi:10.1029/2007GC001743.

Naranjo, J.A., 1987. Interpretacion de la actividad cenozoica superior a lo largo de la Zona de Falla Atacama, Norte de Chile. Revista Geológica de Chile(31), 43–55.

Ortlieb, L., Macharé, J., 1990. Geochronologia y morfoestratigrafia de terrazas marinas del Pleistoceno superior: El caso de San Juan-Marcona, Peru. Boletín de la Sociedad Geológica del Perú 81, 87–106.

Ortlieb, L., Zazo, C., Goy, J., Hillaire-Marcel, C., Ghaleb, B., Cournoyer, L., 1996a. Coastal deformation and sea-level changes in the northern Chile subduction area (23°S) during the last 330 ky. Quaternary Science Reviews 15(8-9), 819–831. doi:10.1016/S0277-3791(96)00066-2.

Ortlieb, L., Zazo, C., Goy, J.L., Dabrio, C., Macharé, J., 1996b. Pampa del Palo: an anomalous composite marine terrace on the uprising coast of southern Peru. Journal of South American Earth Sciences 9(5-6), 367–379. doi:10.1016/S0895-9811(96)00020-X.

Ota, Y., Miyauchi, T., Paskoff, R., Koba, M., 1995. Plio-Quaternary marine terraces and their deformation along the Altos de Talinay, North-Central Chile. Revista Geológica de Chile 22(1), 89–102.

Paris, P.J., Walsh, J.P., Corbett, D.R., 2016. Where the continent ends. Geophysical Research Letters 43(23), 12,208-12,216. doi:10.1002/2016GL071130.

Pedoja, K., Dumont, J.F., Lamothe, M., Ortlieb, L., Collot, J.-Y., Ghaleb, B., Auclair, M., Alvarez, V., Labrousse, B., 2006a. Plio-Quaternary uplift of the Manta Peninsula and La Plata Island and the subduction of the Carnegie Ridge, central coast of Ecuador. Journal of South American Earth Sciences 22(1-2), 1–21. doi:10.1016/j.jsames.2006.08.003.

Pedoja, K., Husson, L., Regard, V., Cobbold, P.R., Ostanciaux, E., Johnson, M.E., Kershaw, S., Saillard, M., Martinod, J., Furgerot, L., Weill, P., Delcaillau, B., 2011. Relative sea-level fall since the last interglacial stage: Are coasts uplifting worldwide? Earth-Science Reviews 108(1-2), 1–15. doi:10.1016/j.earscirev.2011.05.002.

Pedoja, K., Ortlieb, L., Dumont, J.F., Lamothe, M., Ghaleb, B., Auclair, M., Labrousse, B., 2006b. Quaternary coastal uplift along the Talara Arc (Ecuador, Northern Peru) from new marine terrace data. Marine Geology 228(1-4), 73–91. doi:10.1016/j.margeo.2006.01.004.

Pilger, R.H., 1981. Plate reconstructions, aseismic ridges, and low-angle subduction beneath the Andes. Geological Society of America Bulletin 92(7), 448. doi:10.1130/0016-7606(1981)92<448:PRARAL>2.0.CO;2.

Prémaillon, M., Regard, V., Dewez, T.J.B., Auda, Y., 2018. GlobR2C2 (Global Recession Rates of Coastal Cliffs): a global relational database to investigate coastal rocky cliff erosion rate variations. Earth Surface Dynamics 6(3), 651–668. doi:10.5194/esurf-6-651-2018.

Rabassa, J., Clapperton, C.M., 1990. Quaternary glaciations of the southern Andes. Quaternary Science Reviews 9(2-3), 153–174. doi:10.1016/0277-3791(90)90016-4.

Ramos, V.A., Folguera, A., 2009. Andean flat-slab subduction through time. Geological Society, London, Special Publications 327(1), 31–54. doi:10.1144/SP327.3.

Regard, V., Saillard, M., Martinod, J., Audin, L., Carretier, S., Pedoja, K., Riquelme, R., Paredes, P., Hérail, G., 2010. Renewed uplift of the Central Andes Forearc revealed by coastal evolution during the Quaternary. Earth and Planetary Science Letters 297(1-2), 199–210. doi:10.1016/j.epsl.2010.06.020.

Rehak, K., Bookhagen, B., Strecker, M.R., Echtler, H.P., 2010. The topographic imprint of a transient climate episode: the western Andean flank between 15.5° and 41.5°S. Earth Surface Processes and Landforms 35(13), 1516–1534. doi:10.1002/esp.1992.

Rodríguez, M.P., Carretier, S., Charrier, R., Saillard, M., Regard, V., Hérail, G., Hall, S., Farber, D., Audin, L., 2013. Geochronology of pediments and marine terraces in north-central Chile and their implications for Quaternary uplift in the Western Andes. Geomorphology 180-181, 33–46. doi:10.1016/j.geomorph.2012.09.003.

Rohling, E.J., Grant, K., Bolshaw, M., Roberts, A.P., Siddall, M., Hemleben, C., Kucera, M., 2009. Antarctic temperature and global sea level closely coupled over the past five glacial cycles. Nature Geoscience 2(7), 500–504. doi:10.1038/ngeo557.

Rovere, A., Ryan, D., Murray-Wallace, C., Simms, A., Vacchi, M., Dutton, A., Lorscheid, T., Chutcharavan, P., Brill, D., Bartz, M., Jankowski, N., Mueller, D., Cohen, K., Gowan, E., 2020. Descriptions of database fields for the World Atlas of Last Interglacial Shorelines (WALIS). Zenodo. doi:10.5281/ZENODO.3961544.

Ruh, J.B., Sallarès, V., Ranero, C.R., Gerya, T., 2016. Crustal deformation dynamics and stress evolution during seamount subduction: High-resolution 3-D numerical modeling. Journal of Geophysical Research: Solid Earth 121(9), 6880–6902. doi:10.1002/2016JB013250.

Saillard, M., 2008. Dynamique du soulèvement côtier Pléistocène des Andes centrales Etude de l'évolution géomorphologique et datations (10Be) de séquences de terrasses marines (Sud Pérou - Nord Chili), Université Paul Sabatier, Toulouse.

Saillard, M., Hall, S.R., Audin, L., Farber, D.L., Hérail, G., Martinod, J., Regard, V., Finkel, R.C., Bondoux, F., 2009. Non-steady long-term uplift rates and Pleistocene marine terrace development along the Andean margin of Chile (31°S) inferred from 10Be dating. Earth and Planetary Science Letters 277(1-2), 50–63. doi:10.1016/j.epsl.2008.09.039.

Saillard, M., Hall, S.R., Audin, L., Farber, D.L., Regard, V., Hérail, G., 2011. Andean coastal uplift and active tectonics in southern Peru: 10Be surface exposure dating of differentially uplifted marine terrace sequences (San Juan de Marcona, ~15.4°S). Geomorphology 128(3-4), 178–190. doi:10.1016/j.geomorph.2011.01.004.

Santibáñez, I., Cembrano, J., García-Pérez, T., Costa, C., Yáñez, G., Marquardt, C., Arancibia, G., González, G., 2019. Crustal faults in the Chilean Andes: geological constraints and seismic potential. Andean Geology 46(1), 32. doi:10.5027/andgeoV46n1-3067.

Scholl, D.W., Huene, R. von, 2007. Crustal recycling at modern subduction zones applied to the past—Issues of growth and preservation of continental basement crust, mantle geochemistry, and supercontinent reconstruction. In: 4-D Framework of Continental Crust. Geological Society of America, pp. 9–32.

Schwanghart, W., Kuhn, N.J., 2010. TopoToolbox: A set of Matlab functions for topographic analysis. Environmental Modelling & Software 25(6), 770–781. doi:10.1016/j.envsoft.2009.12.002.

Schweller, W.J., Kulm, L.D., Prince, R.A., 1981. Tectonics, structure, and sedimentary framework of the Peru-Chile Trench. Geological Society of America Memoir 154, 323–350. doi:10.1130/MEM154-p323.

Shackleton, N.J., Sánchez-Goñi, M.F., Pailler, D., Lancelot, Y., 2003. Marine Isotope Substage 5e and the Eemian Interglacial. Global and Planetary Change 36(3), 151–155. doi:10.1016/S0921-8181(02)00181-9.

Shepherd, A., Wingham, D., 2007. Recent sea-level contributions of the Antarctic and Greenland ice sheets. Science (New York, N.Y.) 315(5818), 1529–1532. doi:10.1126/science.1136776.

Siddall, M., Chappell, J., Potter, E.-K., 2006. Eustatic sea level during past interglacials. In: Sirocko, F., Litt, T., Claussen, M., Sanchez-Goni, M.-F. (Eds.), The climate of past interglacials. Elsevier, Amsterdam, pp. 75–92.

Simms, A.R., Rouby, H., Lambeck, K., 2016. Marine terraces and rates of vertical tectonic motion: The importance of glacio-isostatic adjustment along the Pacific coast of central North America. Geological Society of America Bulletin, B31299.1. doi:10.1130/B31299.1.

1089 Sobolev, S.V., Babeyko, A.Y., 2005. What drives orogeny in the Andes? Geology 33(8), 617–620.
1090 doi:10.1130/G21557AR.1.

1091 Stern, C.R., 1991. Role of subduction erosion in the generation of Andean magmas. Geology 19(1), 78.
1092 doi:10.1130/0091-7613(1991)019<0078:ROSEIT>2.3.CO;2.

1093 Stewart, I.S., Sauber, J., Rose, J., 2000. Glacio-seismotectonics: ice sheets, crustal deformation and seismicity.
1094 Quaternary Science Reviews 19(14-15), 1367–1389. doi:10.1016/S0277-3791(00)00094-9.

1095 Stirling, C.H., Esat, T.M., Lambeck, K., McCulloch, M.T., 1998. Timing and duration of the Last Interglacial:
1096 evidence for a restricted interval of widespread coral reef growth. Earth and Planetary Science Letters 160(3-4),
1097 745–762. doi:10.1016/S0012-821X(98)00125-3.

1098 Strecker, M.R., Alonso, R.N., Bookhagen, B., Carrapa, B., Hilley, G.E., Sobel, E.R., Trauth, M.H., 2007. Tectonics
1099 and Climate of the Southern Central Andes. Annual Review of Earth and Planetary Sciences 35(1), 747–787.
1100 doi:10.1146/annurev.earth.35.031306.140158.

1101 Suárez, G., Molnar, P., Burchfiel, B.C., 1983. Seismicity, fault plane solutions, depth of faulting, and active
1102 tectonics of the Andes of Peru, Ecuador, and southern Colombia. Journal of Geophysical Research 88(B12),
1103 10403–10428. doi:10.1029/JB088iB12p10403.

1104 Taylor, F.W., Frohlich, C., Lecolle, J., Strecker, M., 1987. Analysis of partially emerged corals and reef terraces in
1105 the central Vanuatu Arc: Comparison of contemporary coseismic and nonseismic with quaternary vertical
1106 movements. Journal of Geophysical Research 92(B6), 4905. doi:10.1029/JB092iB06p04905.

1107 Trenhaile, A.S., 2002. Modeling the development of marine terraces on tectonically mobile rock coasts. Marine
1108 Geology 185(3-4), 341–361. doi:10.1016/S0025-3227(02)00187-1.

1109 Turcotte, D.L., Schubert, G., 1982. Geodynamics: Applications of Continuum Physics to Geological Problema. John
1110 Wiley, New York (450 pp.).

1111 Veloza, G., Styron, R., Taylor, M., Mora, A., 2012. Open-source archive of active faults for northwest South
1112 America. GSA Today 22(10), 4–10. doi:10.1130/GSAT-G156A.1.

1113 Venzke, E., 2013. Volcanoes of the World, v. 4.3.4. Global Volcanism Program.

1114 Victor, P., Sobiesiak, M., Glodny, J., Nielsen, S.N., Oncken, O., 2011. Long-term persistence of subduction
1115 earthquake segment boundaries: Evidence from Mejillones Peninsula, northern Chile. Journal of Geophysical
1116 Research 116(B2), 93. doi:10.1029/2010JB007771.

1117 Villegas-Lanza, J.C., Chlieh, M., Cavalié, O., Tavera, H., Baby, P., Chire-Chira, J., Nocquet, J.-M., 2016. Active
1118 tectonics of Peru: Heterogeneous interseismic coupling along the Nazca megathrust, rigid motion of the
1119 Peruvian Sliver, and Subandean shortening accommodation. Journal of Geophysical Research: Solid Earth
1120 121(10), 7371–7394. doi:10.1002/2016JB013080.

1121 von Huene, R., Corvalán, J., Flueh, E.R., Hinz, K., Korstgard, J., Ranero, C.R., Weinrebe, W., 1997. Tectonic
1122 control of the subducting Juan Fernández Ridge on the Andean margin near Valparaiso, Chile. Tectonics 16(3),
1123 474–488. doi:10.1029/96TC03703.

1124 von Huene, R., Scholl, D.W., 1991. Observations at convergent margins concerning sediment subduction,
1125 subduction erosion, and the growth of continental crust. Geology 29(3), 279. doi:10.1029/91RG00969.

1126 Wang, K., Bilek, S.L., 2011. Do subducting seamounts generate or stop large earthquakes? Geology 39(9), 819–822.
1127 doi:10.1130/G31856.1.

1128 Wang, K., Bilek, S.L., 2014. Invited review paper: Fault creep caused by subduction of rough seafloor relief.
1129 Tectonophysics 610, 1–24. doi:10.1016/j.tecto.2013.11.024.

1130 Watts, A.B., Daly, S.F., 1981. Long Wavelength Gravity and Topography Anomalies. Annual Review of Earth and
1131 Planetary Sciences 9, 415–448.